

# Modulation Strategies and Activity Descriptors of Spinel Electrocatalysts for Lithium–Oxygen Batteries

Yu Pan<sup>+[a]</sup> Ruizhe Xu<sup>+[a]</sup> Anjun Hu,<sup>\*[a, b]</sup> Chuan Zhao,<sup>[a]</sup> Runjing Li,<sup>[a]</sup> Bo Zhou,<sup>\*[a]</sup> Jing Liu,<sup>[a]</sup> and Jianping Long<sup>\*[a]</sup>

The exploitation of high energy density lithium–oxygen batteries (LOBs) holds significant importance for energy storage and applications. An efficient cathode catalyst can effectively prevent the accumulation of the insulating insoluble discharge product  $\text{Li}_2\text{O}_2$ , thereby enhancing the electrochemical performance. Spinel materials, widely available and cost-effective, exhibit superior catalytic activity, making them ideal candidates for LOBs cathode catalysts. This review aims to offer a

comprehensive and insightful overview of the recent progress in the design of spinel-type electrocatalysts for LOBs. This review exhaustively summarizes various modification strategies applied to spinel materials and emphasizes the influential role of catalytic descriptors in designing highly active spinel-type catalysts. This review provides guidance for the design and utilization of high-performance spinel-type catalysts, thereby contributing to the dynamic development of LOBs.

## 1. Introduction

Lithium–oxygen batteries (LOBs) are widely regarded as a promising energy storage device due to their high theoretical energy density ( $3500 \text{ Wh kg}^{-1}$ ).<sup>[1–4]</sup> With respect to the electrolytes used, rechargeable LOBs can be classified into four types,<sup>[5–7]</sup> namely (1) aprotic, (2) aqueous, (3) hybrid aqueous/aprotic, and (4) all-solid-state. It is worth noting that the chemistry of the cathodes of the above systems varies with the electrolyte surrounding the cathode. For the moment, there has been a dominance of research on aprotic LOB, therefore all of the following discussion is all around aprotic LOBs. For clarity, all references to the “LOBs” below are to “aprotic LOBs”. The basic configuration of LOBs consists of a lithium anode, an  $\text{O}_2$  cathode and an electrolyte, as illustrated in Scheme 1.<sup>[8–11]</sup> During the discharge process, Li at the anode undergoes oxidation to form  $\text{Li}^+$  by losing electrons. In the cathode,  $\text{O}_2$  is reduced by gaining electrons and then combines with  $\text{Li}^+$  in the electrolyte to generate the insulating and insoluble discharge product  $\text{Li}_2\text{O}_2$ .<sup>[12–15]</sup> Subsequently, during charging,  $\text{Li}_2\text{O}_2$  loses electrons and decomposes into  $\text{Li}^+$  and  $\text{O}_2$ .<sup>[15–18]</sup> It is crucial to note that the accumulation of  $\text{Li}_2\text{O}_2$  during discharging and its incomplete decomposition during charging give rise to sluggish oxygen reduction reaction/oxygen evolution reaction (ORR/OER) kinetics, leading to poor discharge capacity,

excessive overpotential and unsatisfactory cycling performance for LOBs.<sup>[9,10,19]</sup> In summary, the reversible formation and decomposition of  $\text{Li}_2\text{O}_2$  at the cathode is closely related to the key electrochemical properties of LOBs.

A feasible strategy to address these issues and enhance the electrochemical performance of LOBs, more in-depth exploration and investigation of efficient cathode catalysts.<sup>[20–22]</sup> Generally, cathode catalysts used in LOBs include noble metals, carbon materials, and non-noble metal catalysts. Noble metals, due to their intrinsic half-filled antibonding states, readily enable the modulation of the adsorption strength between the reaction intermediates and catalysts, thus significantly optimizing the ORR/OER catalytic activity.<sup>[23–26]</sup> For instance, PtAu noble-metal-based LOBs, as reported by Guo’s group, demonstrated a low charging overpotential of 0.36 V at a limited capacity of  $1000 \text{ mAh g}^{-1}$  and an excellent cycle life of 220 cycles.<sup>[27]</sup> Despite the excellent electrocatalytic performance, the expensive and rare properties of noble metal catalysts make them unsuitable for wide-scale diffusion.<sup>[28]</sup> Carbon materials, offering adjustable micro-structure and a large specific surface area are suitable cathode catalyst materials.<sup>[29–32]</sup> Cao’s group demonstrated that  $\text{MoO}_x$ -coated carbon nanotubes as the cathode of LOBs had a charging overpotential of only about 0.52 V, with an improved cycle stability of over 210 cycles.<sup>[33]</sup> However, the accumulation of side products resulting from parasitic reactions between carbon and electrolytes often leads to the deterioration and capacity fading of LOBs.<sup>[34,35]</sup> Non-noble metal catalysts, which are abundant and typically includes transition metal oxides, metal nitrides, and metal sulfides, have also garnered attention.<sup>[36–39]</sup> Among them, spinel-type catalysts have received considerable attention owing to their easily adjustable coordination structure and low cost.

Spinel-type materials, denoted as  $\text{AB}_2\text{X}_4$  where A and B stand for metal cations, are characterized by closely packed anions ( $\text{O}^{2-}$ ,  $\text{S}^{2-}$ ...) with  $\text{A}^{2+}$  and  $\text{B}^{3+}$  cations occupying tetrahedral and octahedral positions, respectively.<sup>[40,41]</sup> Moreover, these materials are known for their wide distribution,

[a] Y. Pan,<sup>+[a]</sup> R. Xu,<sup>+[a]</sup> A. Hu, C. Zhao, R. Li, B. Zhou, J. Liu, J. Long  
College of Materials and Chemistry & Chemical Engineering, Chengdu University of Technology, 1#, Dongsanlu, Exianqiao, Chengdu 610059, Sichuan, P. R. China  
E-mail: anjunhu@cdut.edu.cn  
zhanghangzhoubo@163.com  
longjianping@cdut.cn

[b] A. Hu  
College of Computer Science and Cyber Security, Chengdu University of Technology, 1#, Dongsanlu, Exianqiao, Chengdu 610059, Sichuan, P. R. China

[+] These authors contributed to this work equally

long-term stability and environmentally friendliness.<sup>[42–44]</sup> It is well established that the catalytic properties of catalysts are determined by both the number of active sites and intrinsic activity.<sup>[45–47]</sup> Spinel-type materials not only provide abundant active sites, but also possess a tunable coordination structure that can facilitate the enhancement of the intrinsic activity of the active sites. Therefore, these materials serve as ideal electrocatalysts in the context of LOBs. To obtain the desired long-life, low overpotential of LOBs, the rational design of spinel-type catalysts with high catalytic activity are especially significant through modification strategies (doping, vacancy defects, heterostructure) in Scheme 1. Besides, the catalytic descriptors (d-band center, e<sub>g</sub> occupancy, and metal-O covacency) reveal the correlation between the electronic structure of the catalysts and the catalytic behavior, from which spinel-type catalysts with optimal catalytic performance are available. Despite the wide usage of spinel-type materials as cathode catalysts in lithium–oxygen electrochemical systems in recent years, there exists a gap in detailed descriptions within this field. Therefore, a comprehensive summary of the effects of spinel-type catalyst modification strategies and corresponding changes in catalytic descriptors on the performance of LOBs is essential to provide reliable guidance for the design and construction of subsequent high-efficiency spinel-type catalysts.

In this review, we first report in detail the mechanism of action and research progress of spinel-type catalysts in LOBs. Secondly, the modification strategies that effectively optimize the catalytic properties of spinel-type materials are summarized and discussed. These strategies are vital for understanding the interactions between catalysts and reaction intermediates. Subsequently, we highlight the role of catalytic descriptors, which indicate variations in the electronic structure of spinel-type catalysts. Understanding these variations is crucial for a comprehensive exploration of catalyst-reaction intermediate interactions, which greatly promotes the future development and practical application of LOBs.



Yu Pan received his bachelor's degree from Hunan University of Science and Technology and is now a master's candidate at the College of Materials and Chemistry & Chemical Engineering, Chengdu University of Technology. Currently, His current research interest focuses on the design and development of efficient cathode catalysts for lithium–oxygen batteries.



Ruizhe Xu received his bachelor's degree from Chengdu University of Technology and is currently a master's candidate in College of Materials and Chemistry & Chemical Engineering, Chengdu University of Technology. At present, His current research interest is mainly engaged in the development of safe high-performance electrolytes for lithium metal batteries.

## 2. Fundamental Spinel-type Electrocatalysts in LOBs

### 2.1. Mechanisms of LOBs

Existing experiments show that the growth and distribution of the discharge product Li<sub>2</sub>O<sub>2</sub> exerts a tremendous influence on the electrochemical performance of LOBs compared to other batteries.<sup>[57–62]</sup> The growth mechanism of Li<sub>2</sub>O<sub>2</sub> mainly includes surface adsorption mechanism (equal 1–2) and solution-mediated mechanism (equal 3–4).<sup>[17,63–65]</sup> In particular, the key factor affecting the growth of Li<sub>2</sub>O<sub>2</sub> is the solubility of the reaction intermediate LiO<sub>2</sub> in Figure 1a.<sup>[66]</sup> To regulate the LiO<sub>2</sub> solubility in a controllable manner, the role of cathodic catalyst is indispensable.

Surface adsorption mechanism: when the cathode catalyst has strong adsorption, O<sub>2</sub> gains electrons on the electrode surface and combines with Li<sup>+</sup> to form LiO<sub>2</sub><sup>\*</sup> intermediates. Subsequently, the reaction intermediates continue to participate in the reaction at the surface, in which secondary electron transfer occurs, finally causing the generation of thin film-like Li<sub>2</sub>O<sub>2</sub>.<sup>[44,67,68]</sup>



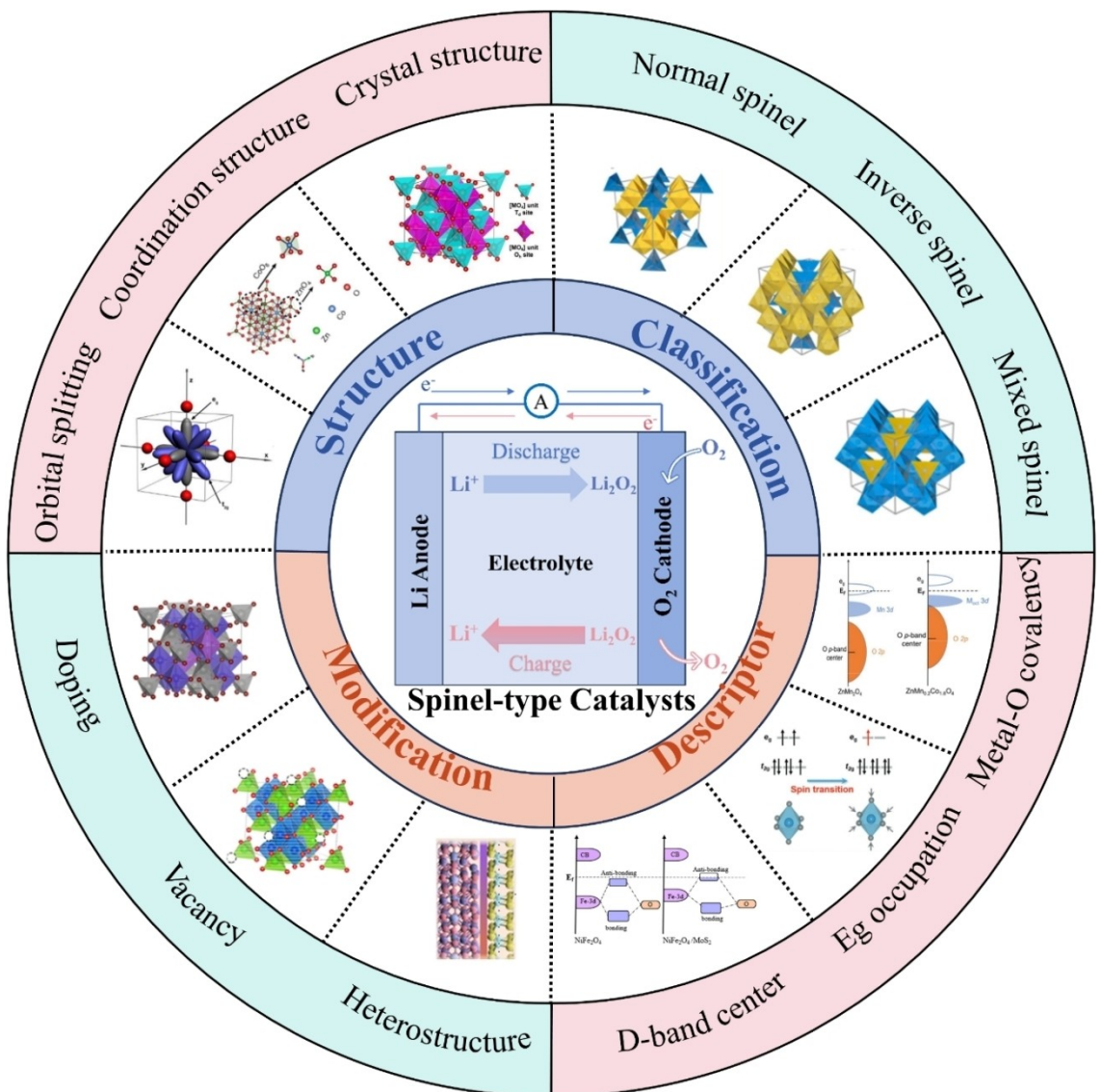
Solution-mediated mechanism: when the cathode catalyst has weak adsorption, the intermediate product LiO<sub>2</sub> generated by O<sub>2</sub> reduction solvates and diffuses into the electrolyte. As the reaction proceeds, the LiO<sub>2</sub>(sol) aggregated in the electrolyte undergoes further disproportionation reactions, resulting in the formation of toroidal Li<sub>2</sub>O<sub>2</sub>.<sup>[69–71]</sup>



Anjun Hu received his Ph. D. degree from University of Electronic Science and Technology of China (UESTC) in 2023. He is currently working at Chengdu University of Technology (CDUT). His research interests have focused on the synthesis-structure-property-mechanism of functional nanomaterials and energy materials and their applications in energy science.



Jianping Long is currently a Professor in the College of Materials and Chemistry & Chemical Engineering at Chengdu University of Technology. His current research interest focuses on basic and applied research of functional materials.



**Scheme 1.** The schematic shows the main topics considered in this paper, revealing the progress of spinel-type catalysts in the system of LOBs research. (Crystal structure. Reproduced with permission.<sup>[48]</sup> Copyright 2020, American Chemical Society. Coordination structure. Reproduced with permission.<sup>[49]</sup> Copyright 2021, Wiley-VCH. Orbital splitting. Reproduced with permission.<sup>[50]</sup> Copyright 2019, Wiley-VCH. Classification. Reproduced with permission.<sup>[51]</sup> Copyright 2023, Elsevier. Doping. Reproduced with permission.<sup>[52]</sup> Copyright 2019, Elsevier. Vacancy. Reproduced with permission.<sup>[53]</sup> Copyright 2017, American Chemical Society. Heterostructure. Reproduced with permission.<sup>[54]</sup> Copyright 2022, Elsevier. Metal–O covalency. Reproduced with permission.<sup>[55]</sup> Copyright 2018, American Chemical Society. E<sub>g</sub> occupation. Reproduced with permission.<sup>[56]</sup> Copyright 2020, Wiley-VCH. D-band center. Reproduced with permission.<sup>[54]</sup> Copyright 2022, Elsevier.)



In summary, the reversible formation and decomposition of Li<sub>2</sub>O<sub>2</sub> having different morphologies enable LOBs to exhibit different electrochemical performances. Film-like Li<sub>2</sub>O<sub>2</sub> has a high contact area with the cathodic surface that enhances charge transfer of both, leading to faster decomposition reactions and reducing charging voltage of LOBs. However, film-like Li<sub>2</sub>O<sub>2</sub> tends to completely cover the cathodic surface, unfavorable to the continued growth of discharge products, resulting in poor LOBs discharge capacity. In contrast, the toroidal Li<sub>2</sub>O<sub>2</sub> possesses less contact area with the cathodic surface but larger voids, thus the corresponding LOBs exhibit

larger discharge capacity but higher overpotential.<sup>[72–74]</sup> As a result, a rational design of high-efficiency cathode catalysts is essential to control the reversible formation of discharge products.

## 2.2. Structure and electrocatalysis of spinel materials

Currently, spinel-type materials are widely applied as powerful catalysts in various research fields based on their stable existence and excellent catalytic properties. The crystal structure of spinel is presented in Figure 1b, where oxygen ions are arranged in a cubic close-packed arrangement while metal ions

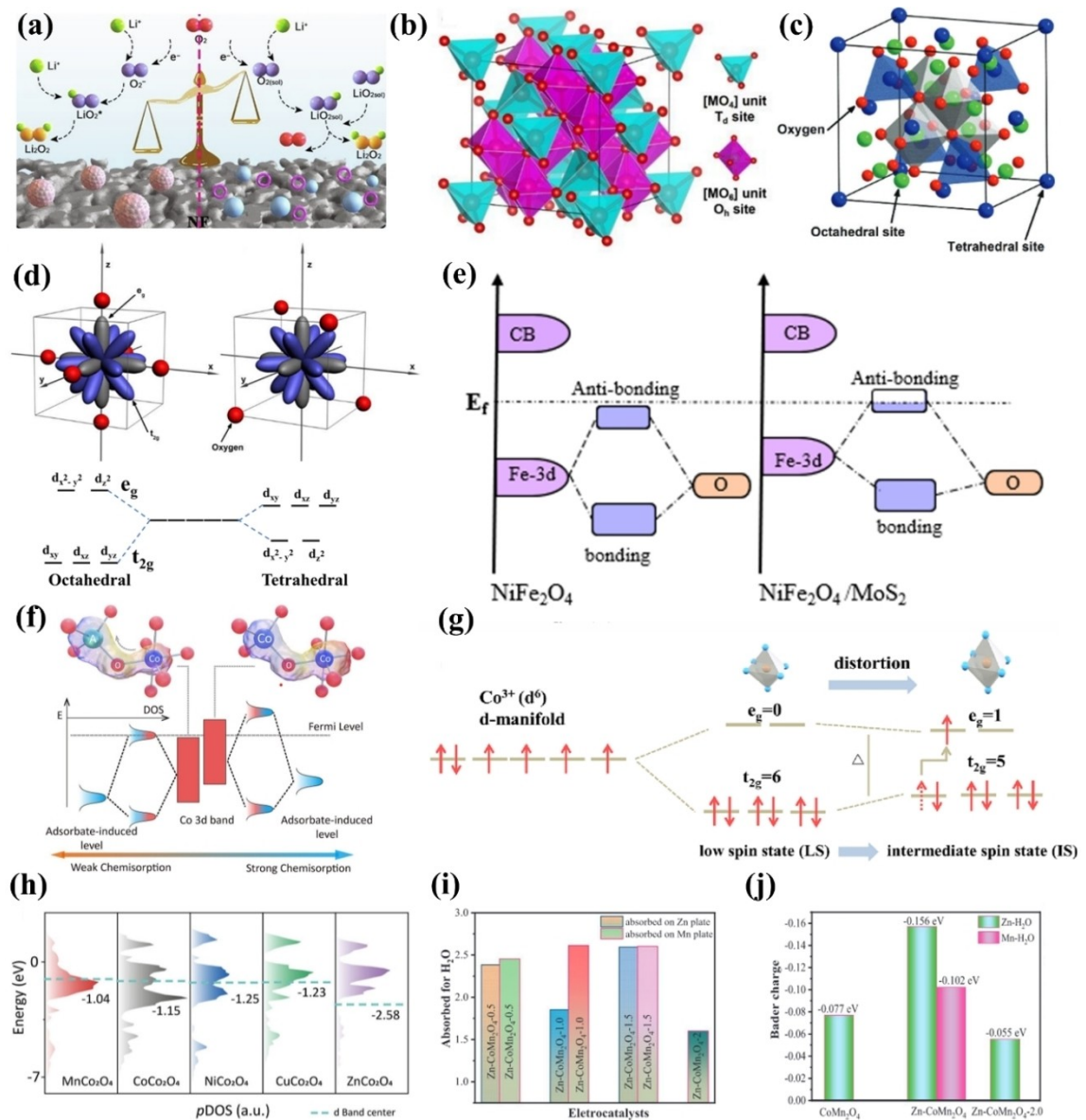


**Figure 1.** (a) Schematic illustration of the formation of discharge products of LOBs. Schematic diagram of (b) spinel crystal structure and (c) distribution of the coordination ions. (d) Metal cation orbital splitting in octahedral and tetrahedral coordination structures in spinel. (e) Bonding effects of spinel with reaction intermediates and (f) corresponding specific effects. (g) Optimization of spinel e<sub>g</sub> orbitals. (h) Projected density of states (PDOS) and d-band centers for various spinel. (i) Comparison of adsorption capacities towards reactants on spinel. (j) Bader charge transfer from the spinel to reactants. (a) Reproduced with permission.<sup>[66]</sup> Copyright 2020 Elsevier. (b) Reproduced with permission.<sup>[48]</sup> Copyright 2020, American Chemical Society. (c) Reproduced with permission.<sup>[40]</sup> Copyright 2017, Wiley-VCH. (d) Reproduced with permission.<sup>[76]</sup> Copyright 2019, Wiley-VCH. (e) Reproduced with permission.<sup>[54]</sup> Copyright 2022 Elsevier Inc. (f, h) Reproduced with permission.<sup>[77]</sup> Copyright 2021, Wiley-VCH. (g) Reproduced with permission.<sup>[78]</sup> Copyright 2023 Elsevier. (i, j) Reproduced with permission.<sup>[79]</sup> Copyright 2022, Wiley-VCH.

fill the tetrahedral and octahedral interstices, respectively.<sup>[48]</sup> Specifically, a spinel cell typically contains 8 divalent cations ( $A^{2+}$ ), 16 trivalent cations ( $B^{3+}$ ), and 32  $O^{2-}$ , described by the general formula  $AB_2O_4$  (Figure 1c).<sup>[40]</sup> Notably, spinel is also classified as normal spinel, anti-spinel and complex spinel according to the distribution of cations. When 32  $O^{2-}$  are cubically dense stacked, 64 tetrahedral voids and 32 octahedral voids are formed for cation filling. For normal spinel, 8  $A^{2+}$  cations fill one-eighth of the tetrahedral voids while 16  $B^{3+}$  cations fill one half of the octahedral voids, expressed as  $(A^{2+})_{th}(B^{3+})_{oh}O_4$ . For anti-spinel, all  $A^{2+}$  cations and half of  $B^{3+}$

cations occupy the octahedral voids, whereas the remaining half of  $B^{3+}$  cations is located in the tetrahedral voids, represented as  $(B^{3+})_{th}(A^{2+})_{oh}(B^{3+})_{oh}O_4$ . For complex spinel, the structure is intermediate between both normal spinel and anti-spinel, both  $A^{2+}$  and  $B^{3+}$  cations partially fill the tetrahedral and octahedral voids, denoted as  $(A^{2+})_{th}(B^{3+})_x(A^{2+})_{oh}(B^{3+})_{oh}O_4$  ( $x=0-1$ ,  $y=0-2$ ).<sup>[51,75,76]</sup> In summary, the spinel with diverse structures tends to exhibit different physicochemical properties, which assist in realizing a wide range of applications for spinel-type catalysts.

Spinel with unique coordination structure presents tunable composition, which allows for easy electronic structure optimization, purposefully enhancing the catalytic performance. For spinel, the bonding interactions between metal cations and oxygen anions vary among different coordination environments, resulting in diverse bond lengths and bond angles. In Figure 1d, when the metal cation combines with six oxygen anions to form a standard octahedron, the original energy-level concatenated d orbitals of the metal cation split, causing a rearrangement of electron.<sup>[76]</sup> When the metal cation combines with six oxygen anions to form a standard octahedron, the d orbitals of the original energy level of the metal cation are split into two groups:  $d_{xy}$ ,  $d_{xz}$ , and  $d_{yz}$  are at the lower energy level, all of which are equal in energy, called  $t_{2g}$  orbitals; similarly, high-energy level  $d_{x^2-y^2}$  and  $d_z^2$  are equal in energy, known as the  $e_g$  orbitals.<sup>[40,76]</sup> Moreover, it is important to note that the electrons in the original d-orbitals are redistributed into the  $t_{2g}$  and  $e_g$  orbitals from low to high according to the lowest-energy principle. When a metal cation combines with four oxygen anions to form a standard tetrahedron, the d orbitals of the original energy level of the metal cation also split into two pairs of orbitals,  $t_{2g}$  and  $e_g$  orbitals, but unlike the above octahedral field, where tetrahedral  $t_{2g}$  orbitals are at the higher energy level and the  $e_g$  orbitals are at the lower energy level. The above description exposes the specific distribution of the internal electronic structure of spinel, which is conducive to the exploration of spinel catalysis from its roots.

Electronic structure rearrangement in spinel tends to alter the original catalytic activity, which optimizes the adsorption capacity of reaction intermediates, further accelerating the reaction kinetics. It can be clearly found in Figure 1e that after the formation of a heterogeneous interface between  $\text{NiFe}_2\text{O}_4$  anti-spinel and  $\text{MoS}_2$ , the  $\text{FeO}_6$  coordination structure is changed, which in turn leads to the rearranging of d-orbital electrons in the Fe active site.<sup>[54]</sup> As a consequence, the d-band center of Fe active site moves to the Fermi energy level ( $E_f$ ), which greatly affects bonding interaction between the Fe active site and the reaction intermediates, eventually accelerating charge transfer of the two and enhancing the reaction kinetics. Furthermore, the replacement of Co tetrahedral sites with foreign A atoms induces changes in the electronic structure of Co octahedral sites in Figure 1f, which finally makes the d-energy band far away from the Fermi energy level, reducing the adsorption capacity for reaction intermediates.<sup>[77]</sup> Moreover,  $\text{Co}^{3+}$  octahedra in  $\text{ZnCo}_2\text{O}_4$  undergo geometrical distortion at high temperatures, which changes the crystal field splitting energy and electron pairing energy, resulting in the electrons leaps from the  $t_{2g}$  orbitals to the  $e_g$  orbitals (Figure 1g).<sup>[78]</sup> Apparently,  $\text{ZnCo}_2\text{O}_4$  exhibits spin polarization, in which the change of spin occupancy in the orbitals promotes the distribution of delocalized electrons, facilitating the acceleration of charge transfer at the oxygen electrode and exhibiting superior catalytic performance. The above description suggests that spinel electronic structure optimization provides a root cause to boost the catalytic activity of spinel.

Intensive analysis of the bonding interaction between spinel and reaction intermediates is essential for accelerating the

reaction kinetics. The projected density of states (PDOS) of different kinds of spinel is shown in Figure 1h, which allows to obtain the position of the corresponding d-band center of spinel.<sup>[77]</sup> Then, the bonding effect is determined by the distance between the d-band center and the  $E_f$ , in which the closer the d-band center is to the  $E_f$ , the stronger the bonding effect is, on the contrary, the weaker the bonding effect is. Different metal active sites in spinel materials have different bonding conditions with the reaction intermediates, thus the reasonable regulation of metal site distribution is beneficial to the improvement of catalytic performance. As shown in Figure 1i, the adsorption energy of the reactants was effectively regulated by Zn-doping  $\text{CoMn}_2\text{O}_4$ . With the gradual increase of Zn doping, the adsorption of reactants on the spinel surface was significantly increased, greatly enhancing the catalytic ability. Furthermore, it was clearly seen that Zn-doped  $\text{CoMn}_2\text{O}_4$  exhibited the best electrocatalytic performance by calculating the Bader charge of the catalyst/adsorbent (Figure 1j), in agreement with the above result.<sup>[79]</sup> In conclusion, spinel catalyst with optimized electronic structure exhibits promising electrocatalytic properties, in which bonding interaction between spinel and reaction intermediates is appropriate, thus contributing to accelerate the charge transfer and eventually achieving improved electrochemical properties.

### 2.3. Common spinel-type electrocatalysts

Spinel-type materials have gained attention as efficient electrocatalysts for enhancing ORR/OER reaction activity. Spinel materials are commonly classified in the isometric crystal system, exhibiting a face-centered cubic stacking arrangement. Specifically, oxygen atoms are arranged vertically and in the order of ABC along the (111) direction. These spinels are typically depicted as octahedral crystals of rhombic dodecahedron forms, characterized by a high degree of crystallinity and strong hardness.<sup>[40,76]</sup> Among them, common spinels are classified into Co-based spinels ( $\text{ACo}_2\text{O}_4$ ), Fe-based spinels ( $\text{AFe}_2\text{O}_4$ ), and Mn-based spinels ( $\text{AMn}_2\text{O}_4$ ) according to the B-site cation sites.<sup>[80–82]</sup> Accordingly, it is expected to deepen the comprehension of different kinds of spinel materials, thus laying a solid foundation for the exploration of more efficient catalysts.

#### 2.3.1. Co-based spinels

Cobalt-based spinel ( $\text{ACo}_2\text{O}_4$ ) is commonly red in color, with the A cation typically occupying a tetrahedral site and the  $\text{Co}^{3+}$  residing in an octahedral site. This material exhibits diverse morphologies such as nanotubes, nanosheets and nanoflowers, each containing a certain amount of void space that facilitates charge transfer and accelerates reaction rates. In the preparation and synthesis of cobalt-based spinel, graphene and carbon filaments are frequently employed as conductive supports. This choice aids in enhancing internal charge transfer, improving electrical conductivity, and increasing the reactive surface

area.<sup>[80–82]</sup> Cobalt-based spinel has received extensive study as a representative of OER spinel. Moreover, Variants of  $\text{ACo}_2\text{O}_4$  typically include  $\text{Co}_3\text{O}_4$ ,  $\text{NiCo}_2\text{O}_4$  and  $\text{MnCo}_2\text{O}_4$ .

Notably, one of the most promising candidates for boosting the OER/ORR electrocatalysis is  $\text{Co}_3\text{O}_4$  owing to its environ-

mentally friendly, low cost, high activity and strong stability in alkaline environments. Zhang et al. successfully reduced the coordination of the Co–O band by electrochemical lithiation of  $\text{Co}_3\text{O}_4$  crystals in Figure 2a and 2b, resulting in a significant increase in oxygen vacancies (octahedral  $\text{Co}^{2+}$  sites).<sup>[83]</sup> The

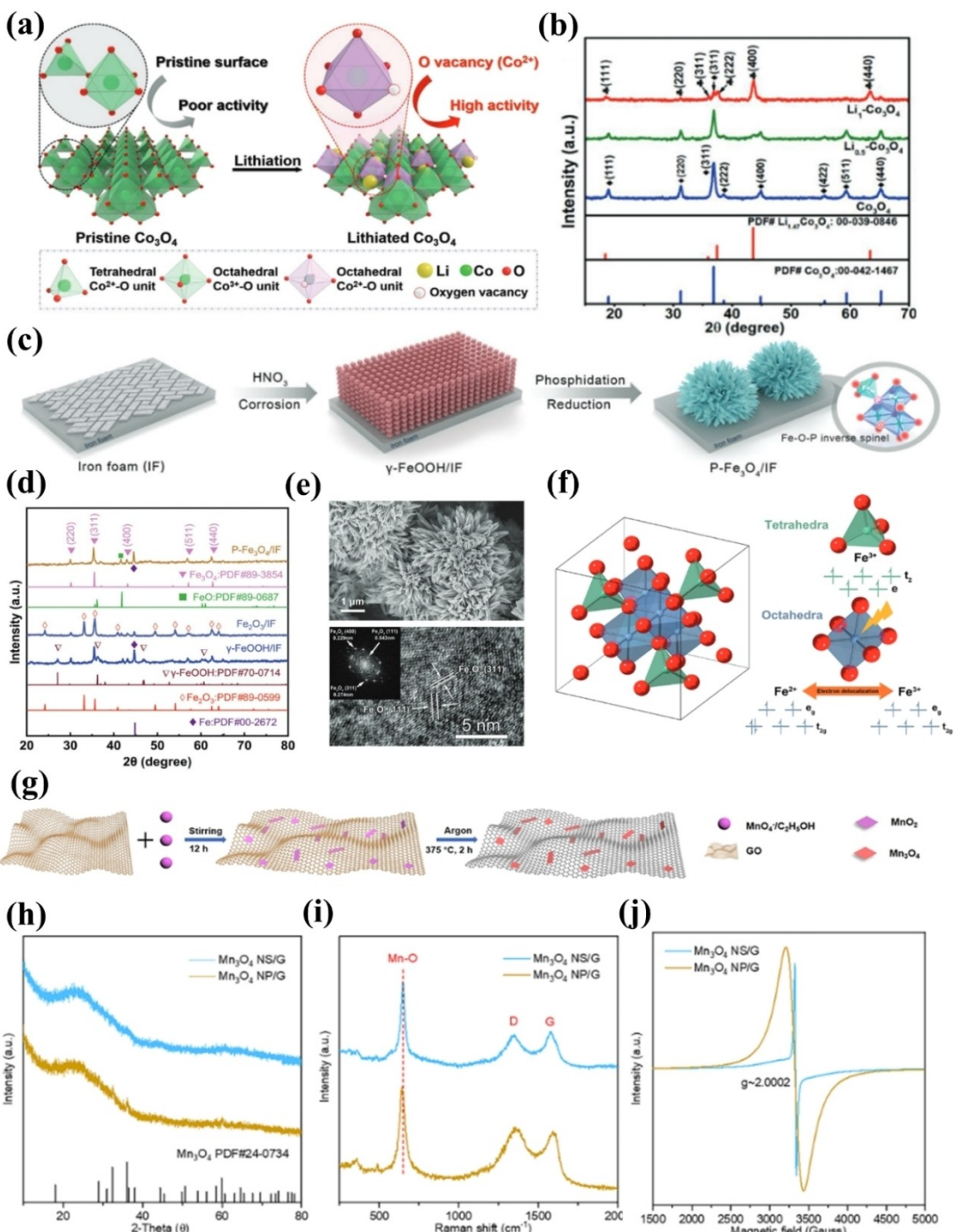


**Figure 2.** (a) Schematic illustration of the preparation of lithiated  $\text{Co}_3\text{O}_4$  through lithiation process. (b) In situ XRD patterns of pristine  $\text{Co}_3\text{O}_4$  and lithiated  $\text{Co}_3\text{O}_4$  with different degrees of lithiation. (c) Schematic diagram of the preparation process of P- $\text{Fe}_3\text{O}_4$ /IF. (d) XRD patterns of P- $\text{Fe}_3\text{O}_4$ /IF (e) SEM image, HRTEM and FFT images of P- $\text{Fe}_3\text{O}_4$ /IF. (f) Schematic orbital splitting and corresponding orbital electron rearrangement of Fe 3d in  $\text{Fe}_3\text{O}_4$  in tetrahedral and octahedral geometrical configurations. (g) The synthesis and characterization of 2D  $\text{Mn}_3\text{O}_4$  NS/G. (h) XRD patterns of  $\text{Mn}_3\text{O}_4$  NS/G and  $\text{Mn}_3\text{O}_4$  NP/G. (i) Raman spectra of  $\text{Mn}_3\text{O}_4$  NS/G and  $\text{Mn}_3\text{O}_4$  NP/G. (j) EPR spectra of  $\text{Mn}_3\text{O}_4$  NS/G and  $\text{Mn}_3\text{O}_4$  NP/G. (a, b) Reproduced with permission.<sup>[83]</sup> Copyright 2020, Wiley-VCH. (c-f) Reproduced with permission.<sup>[84]</sup> Copyright 2019, Wiley-VCH. (g-j) Reproduced with permission.<sup>[85]</sup> Copyright 2022, American Chemical Society.

vacancies further induce the formation of new electronic states in the band gap, which remarkably improves the conductivity and reaction activity of  $\text{Co}_3\text{O}_4$ . Similarly, due to the suitable active area and high catalytic activity of  $\text{Co}_3\text{O}_4$  nanosheets, Liu's group chose them as the substrate for the preparation of highly efficient single-atom catalysts (SAC) in LOBs.<sup>[86]</sup> Specifically, a series of SAC supported by arrays of  $\text{Co}_3\text{O}_4$  nanosheets grown on carbon cloth (labeled MSA  $\text{Co}_3\text{O}_4/\text{CC}$ , M = Ti, V, Cr, Mn, Fe, Ni, Cu, Zn) were synthesized. Experimental results indicate that MSA– $\text{Co}_3\text{O}_4/\text{CC}$  doped with different metal atoms exhibit different electrocatalytic performance for LOBs, providing a direction to investigate the basic catalytic trend of SAC.

In addition to  $\text{Co}_3\text{O}_4$  spinels, other types of Co-based spinels, such as  $\text{ZnCo}_2\text{O}_4$ ,  $\text{NiCo}_2\text{O}_4$  and  $\text{MnCo}_2\text{O}_4$ , have been equally reported as efficient OER catalysts. Highly porous  $\text{ZnCo}_2\text{O}_4$  flowers were successfully synthesized on reduced graphene oxide (RGO) flakes employing a one-step solvothermal method, which exhibits low OER overpotentials and high current densities compared to pristine  $\text{ZnCo}_2\text{O}_4$  spinel.<sup>[87]</sup>  $\text{NiCo}_2\text{O}_4$  nanosheets with oxygen defects and ultrathin structure were rationally designed, in which the ultrathin thickness exposes abundant active sites and the oxygen vacancies improve the electronic structure of the material, successfully optimizing the OER/ORR catalytic performance.<sup>[88]</sup> Peanut-like  $\text{MnCo}_2\text{O}_4$  entangled by multi-walled carbon nanotubes (MCO/MWCNTs) were prepared via a solvothermal method, which presented a unique tertiary mesoporous structure with excellent ORR and OER electrocatalytic activities.<sup>[89]</sup>

### 2.3.2. Fe-based spinels

Iron-based spinel ( $\text{AFe}_2\text{O}_4$ ) is black in color due to the A cation typically occupying a tetrahedral site and the  $\text{Fe}^{3+}$  ion an octahedral site. Its shape is intricately linked to the synthesis process. Through the application of diverse synthesis methods and modification strategies, various morphologies of iron-based spinel, such as nanoparticles and nanorods, have been successfully achieved, enhancing the surface area and boosting the adsorption capacity. Iron-based spinel is commonly prepared and synthesized using carbon nanotubes and carbon cloth as support substrates. This approach not only facilitates the formation of unique nanostructures, but also exposes more active sites, thereby enhancing catalytic performance.<sup>[80–82]</sup> It is important to note that  $\text{AFe}_2\text{O}_4$  is often classified as an anti-spinel, where all  $\text{A}^{2+}$  cations occupy octahedral positions, with half of the  $\text{Fe}^{3+}$  cations distributed in octahedral positions and the remaining half in tetrahedral positions.  $\text{AFe}_2\text{O}_4$  is considered a crucial source of efficient electrocatalysts by virtue of its high electrical conductivity, excellent redox properties, low toxicity and abundant reserves. Notably,  $\text{AFe}_2\text{O}_4$  encompasses  $\text{Fe}_3\text{O}_4$ ,  $\text{NiFe}_2\text{O}_4$  and  $\text{CoFe}_2\text{O}_4$  as typical examples of this family of compounds.

With low cost, simple composition and stable structure,  $\text{Fe}_3\text{O}_4$  presents mixed valence ( $\text{Fe}^{2+}$  and  $\text{Fe}^{3+}$ ), which is favorable for the easy occurrence of redox reactions and provides enough reaction active sites for the adsorption

towards reaction intermediates, representing a valuable cathode catalyst. As shown in Figure 2c, P– $\text{Fe}_3\text{O}_4$  (P– $\text{Fe}_3\text{O}_4/\text{IF}$ ) spinel catalysts with dual active sites in iron foams were successfully prepared by a phosphorus doping modulation strategy.<sup>[84]</sup> In Figure 2d, the successful preparation of P– $\text{Fe}_3\text{O}_4/\text{IF}$  is demonstrated by XRD measurement, in which P– $\text{Fe}_3\text{O}_4$  suffers from lattice expansion due to P-atom doping, with negatively shifted XRD characteristic peaks. As illustrated in Figure 2e, the surface morphology of P– $\text{Fe}_3\text{O}_4/\text{IF}$  was observed to be sea urchin-like nanostructures with a length of about 600 nm and a width of 300 nm by scanning electron microscopy (SEM) images. Moreover, it was also demonstrated in detail by high-resolution transmission electron microscopy (HRTEM) combined with fast Fourier transform (FFT) images of P– $\text{Fe}_3\text{O}_4/\text{IF}$  that the lattice spacing of the (311) and (111) crystal planes are both larger than the original interplanar distances of pure  $\text{Fe}_3\text{O}_4$ . From the above experimental results, it can be found that phosphorus doping modulation enable the coordinated electrons of Fe sites in  $\text{Fe}_3\text{O}_4$  show off-domain, which promotes the rapid inversion of Fe (II) and Fe (III) in  $\text{Fe}_3\text{O}_4$  in the octahedral sites, thus endowing the P– $\text{Fe}_3\text{O}_4$  with metallic properties and high electrical conductivity, as well as facilitates the transfer of electrons in Figure 2f.

In addition to the aforementioned  $\text{Fe}_3\text{O}_4$  anti-spinel,  $\text{NiFe}_2\text{O}_4$  and  $\text{CoFe}_2\text{O}_4$  have generated much interest as efficient catalysts. A series of atomically thin  $\text{NiFe}_2\text{O}_4$  quantum dots (AT  $\text{NiFe}_2\text{O}_4$  QDs) catalysts with different lateral dimensions were controllably synthesized,<sup>[41]</sup> from which it was found that the lateral dimensions of the anti-spinel were negatively correlated with the OER performance. Specifically, the number of low-coordinated oxygen atoms of AT  $\text{NiFe}_2\text{O}_4$  QDs increased with decreasing lateral dimensions, which resulted in a significant increase in the oxygen vacancies and robustly improved the adsorption of the reaction intermediates, yielding OER performances comparable to those of commercial  $\text{RuO}_2$  catalysts. Mao's groups prepared two-dimensional ultrathin  $\text{CoFe}_2\text{O}_4$  nanosheets (NSs) with enriched oxygen vacancies by reducing Prussian blue analogs (PBAs) with  $\text{NaBH}_4$  at room temperature.<sup>[90]</sup> The presence of a large number of oxygen vacancies not only exposes  $\text{CoFe}_2\text{O}_4$  NSs to more reactive active sites and accelerates electron transfer, but also synergizes with  $\text{Co}^{3+}$ , thus dramatically enhancing the  $\text{CoFe}_2\text{O}_4$  OER catalytic activity.

### 2.3.3. Mn-based spinels

Manganese-based spinel ( $\text{AMn}_2\text{O}_4$ ) typically exhibits green or purple colors, with the A cation occupying a tetrahedral site and the  $\text{Mn}^{3+}$  placed in an octahedral site. The morphology of this spinel comprises nanoparticles, nanofibers and necklaces, leading to the exposure of surface atoms and an increase in active sites. In the realm of preparation and synthesis, manganese-based spinel is commonly combined with graphene and nitrogen-doped carbon nanotubes to serve as conductive support. This strategy helps prevent material aggregation, enhances structural stability and improves electrical conductivity.<sup>[80–82]</sup> In comparison with the other categories

mentioned above,  $\text{AMn}_2\text{O}_4$  has been less reported as an electrocatalyst, but still promotes the exploitation of OER catalysts.  $\text{AMn}_2\text{O}_4$  generally exhibits the advantages of various crystal structures, low cost, wide distribution and excellent Jahn-Teller effect. Moreover,  $\text{AMn}_2\text{O}_4$  typically include  $\text{Mn}_3\text{O}_4$ ,  $\text{NiMn}_2\text{O}_4$  and  $\text{CoMn}_2\text{O}_4$ .

$\text{Mn}_3\text{O}_4$  spinel, which is inexpensive and easy to synthesize, represents the most stable manganese oxide in alkaline environments, thus being a promising electrocatalyst. Bao et al. constructed ultrathin  $\text{Mn}_3\text{O}_4$  nanosheets (NS) with (101) crystalline facets on the surface of conductive graphene ( $\text{Mn}_3\text{O}_4$  NS/G) as powerful oxygen cathode catalysts for boosting the electrochemical performance of LOBs in Figure 2g.<sup>[85]</sup> It is observed in Figure 2h that  $\text{Mn}_3\text{O}_4$  NS/G show more diffuse diffraction peaks compared to  $\text{Mn}_3\text{O}_4$  nanoparticles on graphene ( $\text{Mn}_3\text{O}_4$  NP/G) in XRD analysis because of the ultrathin two-dimensional structure. Raman spectroscopy tests effectively verify whether the  $\text{Mn}_3\text{O}_4$  NS/G is prepared. In Figure 2i, there are three obvious characteristic peaks located at  $650 \text{ cm}^{-1}$ ,  $1350 \text{ cm}^{-1}$  and  $1588 \text{ cm}^{-1}$ , which represent the vibration peaks of Mn–O, and the D and G bands of graphene, respectively, fully indicating the successful hybridization of graphene and  $\text{Mn}_3\text{O}_4$ . Furthermore, in order to distinguish the difference between the  $\text{Mn}_3\text{O}_4$  NS/G and  $\text{Mn}_3\text{O}_4$  NP/G, the EPR spectra (Figure 2j) were performed. It can be found that the EPR spectrum of  $\text{Mn}_3\text{O}_4$  NS/G displays a sharp peak at  $g \approx 2$ , whereas  $\text{Mn}_3\text{O}_4$  NP/G reveals only asymmetric broad peaks, which suggests that certain oxygen defects exist in  $\text{Mn}_3\text{O}_4$  NS/G. The experimental results demonstrate that the  $\text{Mn}_3\text{O}_4$  NS/G with exposed (101) crystal surface possesses abundant oxygen vacancies, which facilitates the adsorption and desorption of the reaction intermediates, thus accelerating the OER/ORR reaction kinetics and greatly enhancing the electrochemical performance of LOBs.

Apart from  $\text{Mn}_3\text{O}_4$ ,  $\text{AMn}_2\text{O}_4$  commonly consists of  $\text{CoMn}_2\text{O}_4$  and  $\text{NiMn}_2\text{O}_4$ . For  $\text{CoMn}_2\text{O}_4$ , both  $\text{Co}^{2+}$  and  $\text{Mn}^{3+}$  tend to occupy octahedral and tetrahedral positions simultaneously. Several Zn-doped  $\text{CoMn}_2\text{O}_4$  catalysts with abundant oxygen vacancies were prepared using a simple hydrothermal growth method.<sup>[79]</sup> Theoretical calculations indicated that appropriate doping of Zn ions enhances the density of states of p electrons on the catalyst surface and facilitates the d-band center moving closer to the Fermi energy level, which accelerates the charge transfer rate and optimizes the adsorption free energy for reaction intermediates, eventually enhancing the intrinsic electrocatalytic activity to a large extent. Flaky and spherical  $\text{NiMn}_2\text{O}_4$  grown on Ni foams were successfully constructed by microwave synthesis at  $150^\circ\text{C}$  and  $175^\circ\text{C}$ , respectively.<sup>[91]</sup> Both differently shaped  $\text{NiMn}_2\text{O}_4$  catalysts possess low OER overpotentials under alkaline conditions as well as exhibit excellent catalytic performance, which promotes the development of low-cost and high-performance electrocatalysts without binders.

### 3. Modification strategy for Spinel-type Electrocatalysts

#### 3.1. Doping Modification

The A/B site cations in  $\text{AB}_2\text{O}_4$  can be replaced by other cations with different radius and electronegativities, which can induce spin redistribution of orbital electrons in the surrounding octahedral ligand field and change the electronic properties and surface redox properties, thus enabling the enhancement of the catalytic performance of the spinel material.<sup>[92,93]</sup> For instance, Ren's group effectively altered the electronic structure of the electrocatalysts to improve the catalytic activity for the oxygen electrode reaction by Fe doping spinel Ni–Co oxides.<sup>[94]</sup> As shown in Figure 3a, Fe atoms tend to be doped into the tetrahedral sites in  $\text{NiCo}_2\text{O}_4$  anti-spinel (NCO) to modulate the electronic structure of Ni sites and Co sites, resulting in the formation of high-efficiency electrocatalysts (NCFO). NCFO-based LOBs exhibit higher discharge specific capacity compared to NCO-based and SP-based in Figure 3b, effectively demonstrating the optimization of Fe doping on the electrocatalytic activity of the catalysts. Theoretical calculations revealed that Fe doping reduced  $\eta_{\text{OER}}$  and  $\eta_{\text{ORR}}$  in the electrochemical reaction, indicating an improvement in the catalyst bifunctional catalytic activity in Figure 3c. Moreover, enhanced adsorption of the oxygen-containing intermediate  $\text{LiO}_2$  on the NCFO surface (Figure 3d) promotes the generation of film-like  $\text{Li}_2\text{O}_2$  discharge products by the surface adsorption growth pathway, which ensures that the discharge products possess sufficient contact interfaces with the electrodes to facilitate fast reaction kinetics and charge transfer.

On the basis of the introduction of foreign atoms, doping modification effectively improves the coordination environment of the spinel material itself and enhances the redox capacity of the active sites.  $\text{Co}_{2.85}\text{Mn}_{0.15}\text{O}_4$  as an efficient cathode catalyst was prepared for LOBs by employing a simple solvothermal calcination strategy.<sup>[21]</sup> As seen in Figure 3e,  $\text{Co}_{2.85}\text{Mn}_{0.15}\text{O}_4$  features an atypical spinel stabilized structure, in which Mn atoms replace some of the  $\text{Co}^{3+}$  octahedral sites, not only enhancing the extremely high surface  $\text{Co}^{3+}$  concentration, but also facilitating the surface aggregation of Mn-active species. As a result, surface electron reconstitution effect is more likely to occur during subsequent charging and discharging processes. In Figure 3f, it can be clearly seen that  $\text{Co}_{2.85}\text{Mn}_{0.15}\text{O}_4$  exhibits a significant  $\text{Co}^{3+}/\text{Co}^{2+}$  reversible displacement. After charging, the decrease in the valence of  $\text{Co}^{3+}$  on the electrode surface indicates that  $\text{Co}^{3+}$  is the active site of the OER, where part of the  $\text{Co}^{3+}$  active site will become a temporary  $\text{Co}^{2+}$  site. Then, after the discharge reaction, the area ratio of  $\text{Co}^{3+}/\text{Co}^{2+}$  returned to 1.72, indicating that the temporary  $\text{Co}^{2+}$  sites returned to  $\text{Co}^{3+}$  after discharge, which fully demonstrated the surface electronic structure reconstruction effect of  $\text{Co}_{2.85}\text{Mn}_{0.15}\text{O}_4$  during the charging and discharging of LOBs. The Mn doping enhanced the electron reconstruction effect on the electrode surface, contributing to the improved performance of LOBs. Compared with other comparison groups,  $\text{Co}_{2.85}\text{Mn}_{0.15}\text{O}_4$

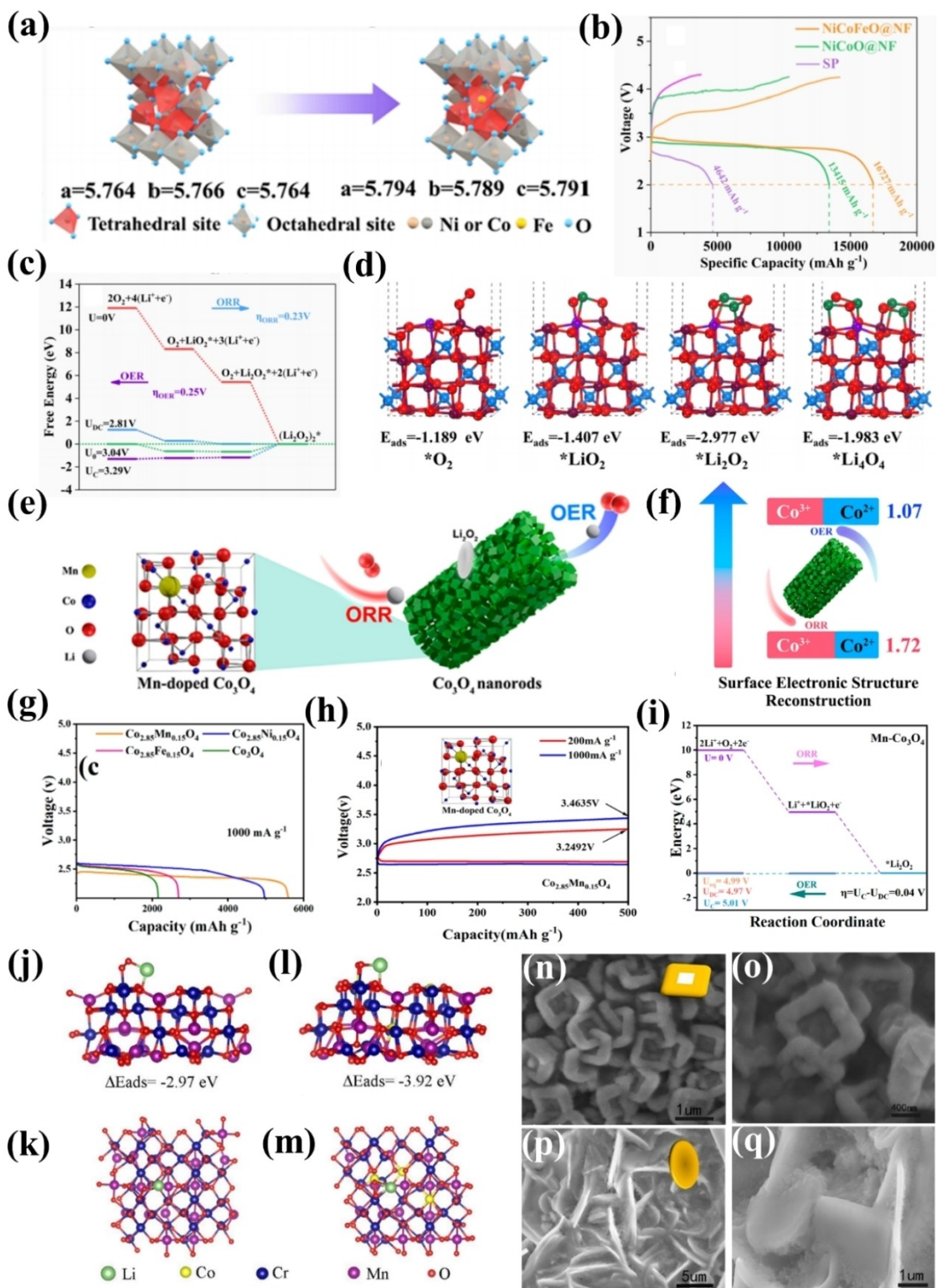


**Figure 3.** (a) Schematic illustration of transformation from  $\text{NiCoO}$  to  $\text{NiCoFeO}$ . (b) The galvanostatic discharge curves of  $\text{NiCoO}$ ,  $\text{NiCoFeO}$  and SP. (c) Free energies of  $\text{NiCoFeO}$ . (d) The optimized structures and the corresponding binding energies of  $\text{O}_2$ ,  $\text{LiO}_2$ ,  $\text{Li}_2\text{O}_2$  and  $\text{Li}_4\text{O}_4$  on the  $\text{NiCoFeO}$  surface. (e) Schematic illustration of the synthesis of  $\text{Co}_{2.85}\text{Mn}_{0.15}\text{O}_4$ . (f) Schematic diagram of surface electronic structure reconstruction phenomenon in ORR and OER processes. (g) Initial discharge curves of four samples at  $1000 \text{ mA g}^{-1}$ . (h) The charge and discharge curves at  $200 \text{ mA g}^{-1}$  and  $1000 \text{ mA g}^{-1}$  for  $\text{Co}_{2.85}\text{Mn}_{0.15}\text{O}_4$ . (i) The reaction free energy for the  $\text{Mn-Co}_3\text{O}_4$  ( $\text{Co}_{2.85}\text{Mn}_{0.15}\text{O}_4$ ). Optimized structures of  $\text{LiO}_2$  adsorbed on the (j, k)  $\text{MnCrO}$  (100) plane, (l, m)  $\text{MnCoCrO}$  (100) plane. Ex situ SEM images of fully discharged (n-o)  $\text{MnCoCrO}$  and (p-q)  $\text{MnCrO}$ -based electrodes with different magnifications. (a-d) Reproduced with permission.<sup>[94]</sup> Copyright 2021, Elsevier. (e-i) Reproduced with permission.<sup>[21]</sup> Copyright 2023, American Chemical Society. (j-q) Reproduced with permission.<sup>[95]</sup> Copyright 2023, Royal Society of Chemistry.

obtained the highest initial discharge capacity ( $5598 \text{ mAh g}^{-1}$ ) at  $1000 \text{ mA g}^{-1}$  and significantly lower overpotentials at  $200 \text{ mA g}^{-1}$  and  $1000 \text{ mA g}^{-1}$  in Figure 3g–3 h. In addition, the free energy diagram of the catalyst obtained by DFT calculations shows that  $\text{Mn}-\text{Co}_3\text{O}_4$  has a remarkably low overpotential (0.04 V), which further verifies that  $\text{Mn}^{3+}$  doping substantially enhances the OER activity of  $\text{Co}_{2.85}\text{Mn}_{0.15}\text{O}_4$  (Figure 3i). In conclusion, the introduction of Mn atoms using a surface electronic structure modification strategy effectively improves the performance of LOBs, which is of significance for the promotion of spinel-type catalysts.

Doping modification adjusts the electron density near the metal ions in the pristine lattice, which takes a significant effect on the catalytic behaviors of active sites. Co-doped  $\text{MnCr}_2\text{O}_4$  ( $\text{MnCoCrO}$ ) with a layered structure was successfully prepared using a combination of sol-gel and annealing methods.<sup>[95]</sup> As shown in the Figure 3j–3 m, Co doping allows the adsorption capacity of the active site on the oxygen-containing intermediate  $\text{LiO}_2$  to be significantly improved, so that the subsequent discharge product  $\text{Li}_2\text{O}_2$  nucleates and grows on the catalyst surface by surface adsorption mechanism, which avoids the dissolution of  $\text{Li}_2\text{O}_2$  into the electrolyte, and effectively inhibits the parasitic reaction caused by the nucleophilic attack of  $\text{LiO}_2$ . The microscopic morphology of  $\text{MnCoCrO}$  and  $\text{MnCrO}$  electrode discharge products was further observed by non-in situ scanning electron microscopy in Figure 3n–3q. For  $\text{MnCoCrO}$ , after discharge, the square ring-shaped  $\text{Li}_2\text{O}_2$  is tightly deposited on the electrode surface, where sufficient contact between  $\text{Li}_2\text{O}_2$  and  $\text{MnCoCrO}$  guarantees that the active sites are in full action and effectively promotes the rapid transport of  $\text{Li}^+$  and electrons, facilitating the reversible decomposition of the discharge products during subsequent charging. For  $\text{MnCrO}$ , the discharge product after discharge is inserted into the cathode in a sheet-like structure. It is worth noting that the sheet-like embedded  $\text{Li}_2\text{O}_2$  cannot fully contact with the active site, which reduces the oxygen and electron transport rate in

the reaction, makes the subsequent decomposition of the discharge product difficult, leading to an excessive charging overpotential and incomplete decomposition of the discharge product. The above results further verified that the discharge products on the  $\text{MnCoCrO}$  electrode with surface adsorption mechanism can fully and reversibly form and decompose, thus greatly enhancing the electrochemical performance of LOBs. In summary, doping modification changes the original crystalline phase structure of spinel catalysts, which in turn modulates the electron distribution in the catalysts, thus optimizing the active site electrocatalytic performance. The electrochemical properties of correlation doped modified spinel in LOBs are shown in Table 1.

### 3.2. Vacancy Defects

The vacancy defects in  $\text{AB}_2\text{O}_4$  spinel can effectively regulate the coordination environment and electronic structure of the active site, which has a significant contribution towards the enhancement of the catalytic activity of the material.<sup>[99–101]</sup> Specifically, vacancy defect engineering involves the removal of small amounts of metal cations (cationic defects) or oxygen anions (anionic defects) in  $\text{AB}_2\text{O}_4$  to achieve a change in physicochemical properties of original spinel, which accelerates the rate of electron transfer and modulates the adsorption capacity of the intermediates in the reaction, providing a viable direction to obtain high-efficiency electrocatalysts. Typically, inducing cation vacancy defects in spinel significantly modulates its electronic structure, optimizes the density of states (DOS) near the Fermi energy level, and accelerates the charge transfer rate, eventually enhancing the OER reaction kinetics to large extent. For instance, Liu et al. initially synthesized glycerolatocobalt (GlyCo) nanostructures with repeating  $\text{Co}-\text{O}-\text{Co}-\text{O}$  units by a hydrothermal method, upon which subsequent heat treatment was carried out to successfully

**Table 1.** Electrochemistry performance of recently reported common spinels with doping modifications in LOBs.

Electrocatalysts	Modification strategies	Specific capacity	Overpotential	Cycle ability	Ref.
$\text{NiCo}_2\text{O}_4$	Fe Doping	$16722 \text{ mAh g}^{-1}$	–	790 h at $500 \text{ mA g}^{-1}$	[94]
$\text{Co}_3\text{O}_4$	Mn Doping	$5598 \text{ mAh g}^{-1}$	–	100 cycles at $1000 \text{ mA g}^{-1}$	[21]
$\text{MnCr}_2\text{O}_4$	Co Doping	$13600 \text{ mAh g}^{-1}$	0.89 V	1000 h at $400 \text{ mA g}^{-1}$	[95]
$\text{Mn}_3\text{O}_4$	Cr Doping	$22,288 \text{ mAh g}^{-1}$	0.86 V	740 h at $200 \text{ mA g}^{-1}$	[96]
$\text{ZnCo}_2\text{O}_4$	Cu Doping	$12984.9 \text{ mAh g}^{-1}$	1.15 V	400 cycles at $200 \text{ mA g}^{-1}$	[97]
$\text{CoFe}_2\text{O}_4$	Cr Doping	$22030 \text{ mAh g}^{-1}$	0.48 V	500 cycles at $300 \text{ mA g}^{-1}$	[98]

obtain cobalt oxide ( $\text{Co}_{3-x}\text{O}_4$ ) with cationic vacancies in Figure 4a.<sup>[102]</sup> The presence of cobalt ion vacancies leads to the non-localization of charge distribution and the reduction of adsorption energy difference between the reaction intermediates, which improves the charge transfer rate and optimizes the adsorption capacity of oxygen-containing intermediates  $\text{LiO}_2$ , practically boosting the electrocatalytic performance of the

catalysts. As a result, the LOBs with excellent electrocatalytic properties of  $\text{Co}_{3-x}\text{O}_4$  cathode catalysts exhibit superior specific capacity, lower overpotential and stable cycling performance. In addition, Zheng's groups similarly accelerated the OER reaction kinetics through the introduction of Co cation vacancy defects on the  $\text{NiCo}_2\text{O}_4$  spinel catalyst, which facilitated the emergence of charge off-domains and optimized the intrinsic conductivity

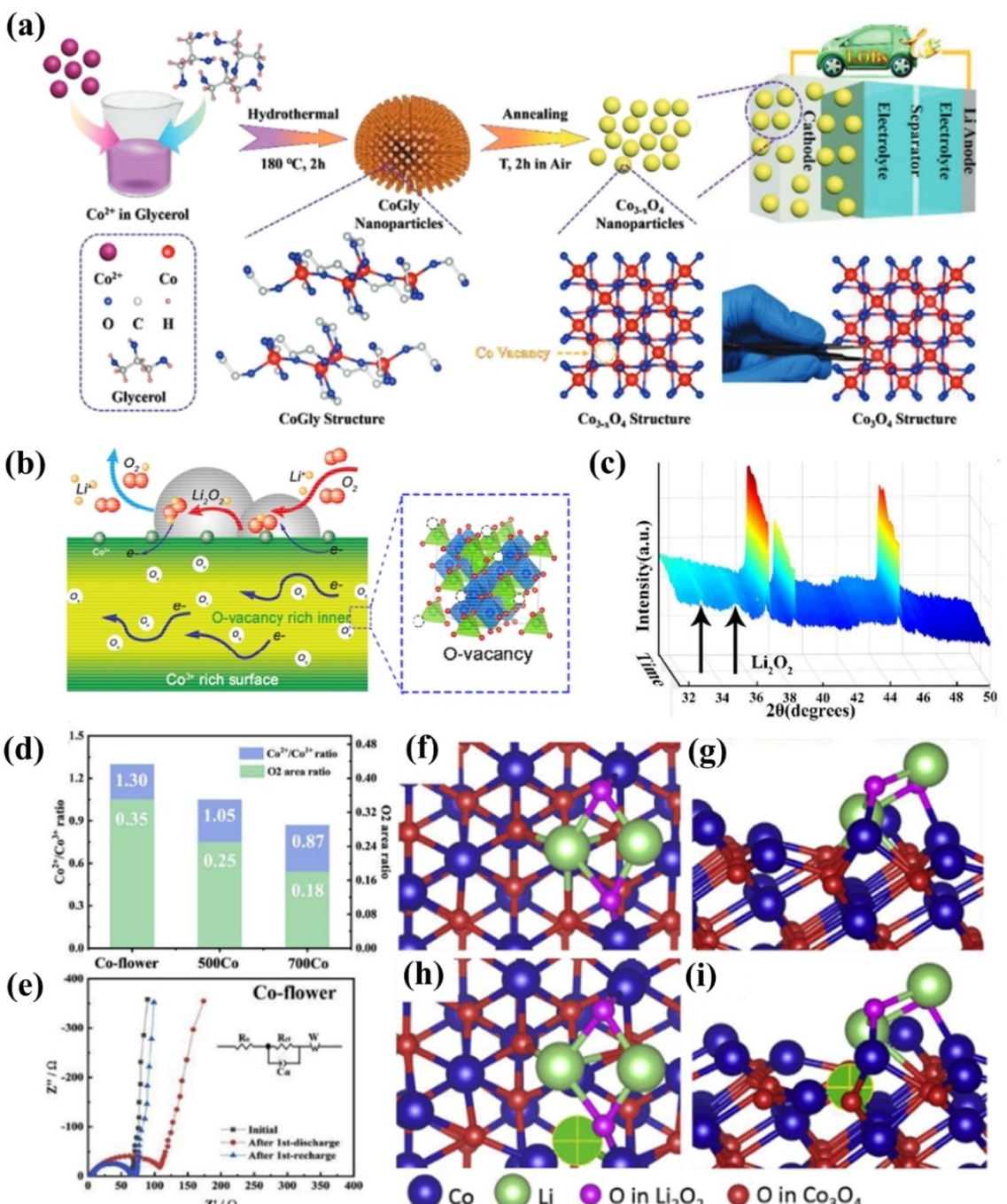


**Figure 4.** (a) Schematic illustration for the preparation process of  $\text{Co}_3\text{O}_4$  with cationic vacancies. (b) Schematic illustration of the synergistic effect of high concentration of oxygen vacancies in the  $\text{Co}_3\text{O}_4$  interior and high  $\text{Co}^{3+}$  concentration on the  $\text{Co}_3\text{O}_4$  surface. (c) Three-dimensional discharge plots of the XRD patterns for  $\text{Co}_3\text{O}_4$  nanosheets, with a constant current of  $200 \text{ mA g}^{-1}$ . (d) The comparison of oxygen vacancies concentration and  $\text{Co}^{2+}/\text{Co}^{3+}$  ratio of Co-flower, 500Co, and 700Co. (e) Nyquist plots of Co-flower catalyzed LOBs at initial, 1st discharge, and 1st charge. (f–g)  $\text{Li}_2\text{O}_2$  cluster adsorption on  $\text{Co}_3\text{O}_4$  (111) surface, (h–i)  $\text{Li}_2\text{O}_2$  cluster adsorption on  $\text{Co}_3\text{O}_4$  (111) surface with  $\text{O}_v$ . (a) Reproduced with permission.<sup>[102]</sup> Copyright 2020 Wiley-VCH. (b–c) Reproduced with permission.<sup>[53]</sup> Copyright 2017, American Chemical Society. (d–i) Reproduced with permission.<sup>[104]</sup> Copyright 2019, Elsevier.

of the catalysts.<sup>[103]</sup> In summary, cationic vacancy defects effectively regulate the physicochemical properties of spinel materials, enhance their intrinsic conductivity and optimize the adsorption capacity of oxygen-containing intermediates in electrochemical reactions, making an important contribution to the exploitation of high-efficiency OER electrocatalysts.

In contrast to cationic vacancies, anionic vacancy defects (oxygen vacancies) in spinel have been extensively studied owing to their lower formation energies and easy and controllable generation. The introduction of oxygen vacancies into spinel increases the charge density around the metal sites, which achieves electron rearrangement and energy gap state modulation on the spinel surface, greatly improving the electrocatalytic activity of the spinel material. Recently, Wang et al. proposed to improve the electrocatalytic activity of  $\text{Co}_3\text{O}_4$  nanosheets by adjusting their internal oxygen vacancy concentration and external  $\text{Co}^{3+}/\text{Co}^{2+}$  ratio for obtaining high-performance and long-life LOBs.<sup>[53]</sup> As illustrated in Figure 4b, it can be clearly seen that the abundant oxygen vacancies existing inside the  $\text{Co}_3\text{O}_4$  nanosheets serve as active sites for binding with  $\text{O}_2$  and the discharge product  $\text{Li}_2\text{O}_2$  during the ORR/OER process, which greatly accelerates the transfer of electrons and  $\text{Li}^+$ , facilitating the reversible formation and decomposition of the discharge product  $\text{Li}_2\text{O}_2$ . In-situ XRD measurements of the electrodes were carried out at different times to further investigate the formation of discharge products  $\text{Li}_2\text{O}_2$  during the discharge process in Figure 4c. With the increase of the discharge time, more distinct peaks at  $2\theta = 32.6^\circ$  and  $34.8^\circ$  gradually appeared in the XRD plots, which refer to the (200) and (201) crystalline peaks of  $\text{Li}_2\text{O}_2$ , respectively, fully demonstrating the generation of the discharge product  $\text{Li}_2\text{O}_2$ . It is worth noting that the simultaneous appearance of the  $32.6^\circ$  and  $34.8^\circ$  peaks suggests that  $\text{Li}_2\text{O}_2$  grows in a non-directional direction, forming an amorphous film first, and then the diffraction peaks gradually broaden as the discharge proceeds, representing the emergence of crystalline flake products, which contribute to the excellent reversibility properties. Furthermore, the appearance of oxygen vacancies in spinel tends to make abundant electronic states near the Fermi energy level in the DOS and induces the appearance of additional donor energy levels. Long's group comprehensively explored the relationship between the concentration of oxygen vacancies in  $\text{NiCo}_2\text{O}_4$  spinel and the catalytic activity of LOBs by modulating them through magnetron sputtering.<sup>[105]</sup> Oxygen vacancies in  $\text{NiCo}_2\text{O}_4$  spinel promote the upward shift of antibonding orbitals in catalytic bonding and provide additional electronic states around  $E_F$ , which optimizes oxygen adsorption in ORR reaction and accelerates the charge transfer rate. Nevertheless, too large a concentration of oxygen vacancies destabilizes the crystal structure and weakens the ability to capture electrons in the  $\text{Li}_2\text{O}_2$  antibonding orbitals, resulting in poor catalytic activity for the OER process. In summary, the optimal oxygen vacancy concentration serves as a critical factor in improving the catalytic activity of the spinel material as a catalyst for LOBs.

On this basis, the oxygen vacancy modification of  $\text{Co}_3\text{O}_4$  with different morphologies can be further carried out to explore the role of oxygen vacancies in depth.  $\text{Co}_3\text{O}_4$  nano-

flowers (Co-flower) with abundant oxygen vacancies were prepared by simple  $350^\circ\text{C}$  heat treatment.<sup>[104]</sup> Co-flower features a unique porous 3D structure, which not only provides sufficient diffusion paths for  $\text{O}_2$  and electrolyte, but also provides enough storage space for the discharge product  $\text{Li}_2\text{O}_2$ , promoting the reversible formation and decomposition of  $\text{Li}_2\text{O}_2$ . Notably, compared with thermolyzed  $\text{Co}_3\text{O}_4$  obtained from high-temperature annealing treatment, more  $\text{Co}^{3+}$  on the Co-flower is reduced to  $\text{Co}^{2+}$ , which is conducive to the generation of oxygen vacancies, accelerating the OER/ORR reaction kinetics and enhancing the cycle life of LOBs (Figure 4d). Impedance variation of Co-flower after charging and discharging were obtained by electrochemical impedance spectra (EIS) test in Figure 4e. Obviously, an increase in the impedance of Co-flower after discharge can be observed, indicating the formation of  $\text{Li}_2\text{O}_2$ , while the impedance basically returns to the initial state after charging, indicating the thorough decomposition of  $\text{Li}_2\text{O}_2$ . The above results fully demonstrate that Co-flower possesses the excellent reversible performance. The specific role of oxygen vacancies in electrochemical reactions was further revealed by DFT calculations. Figure 4f–4g illustrate the  $\text{Li}_2\text{O}_2$  adsorption structure on original  $\text{Co}_3\text{O}_4$  (111) surface. The oxygen atom in  $\text{Li}_2\text{O}_2$  binds to the surface Co, and one of the Li ions is attached to the surface O. In Figure 4h–4i, the binding of Li ions to surface oxygen is changed owing to the presence of surface oxygen vacancies, thereby optimizing the adsorption of  $\text{Li}_2\text{O}_2$ . The presence of surface oxygen vacancies enhances the adsorption capacity of  $\text{Li}_2\text{O}_2$  clusters on the  $\text{Co}_3\text{O}_4$  (111) surface, which allows  $\text{Li}_2\text{O}_2$  to wet the substrate and grow as a nanofilm, that contributes to the full contact of the active sites with the discharge products, thus exhibiting good reversible performance. The nanofilm  $\text{Li}_2\text{O}_2$  is in sufficient contact with the active sites to accelerate the charge transfer rate, thus facilitating the reversible decomposition of the discharge products. In summary, the anionic vacancy defects cause electron rearrangement on the surface of the spinel material, which optimizes its adsorption capacity towards the reaction intermediate, thereby speeding up the OER/ORR reaction kinetic and achieving high-performance and long-life LOBs. The electrochemical properties of the relevant vacancy-modified spinel in LOBs are shown in Table 2.

### 3.3. Heterostructure engineering

Heterostructure engineering is the combination of different solid materials to achieve the complementary advantages among each other.<sup>[73,109,110]</sup> It is worth noting that different components in the heterostructure have different electronic structures, so the built-in electric field is spontaneously formed between them, which induces the transfer and balance of charges at both ends of the interface, accelerating the interfacial charge transfer rate on the one hand, and optimizing the electronic structure of the active site to regulate the adsorption capacity for the reaction intermediates on the other hand. Currently, there is a great deal of interest in composing

**Table 2.** Electrochemistry performance of recently reported common spinels with vacancy modifications in LOBs.

Electrocatalysts	Modification strategies	Specific capacity	Specific capacity	Cycle ability	Ref.
NiFe <sub>2</sub> O <sub>4</sub>	Ni Vacancy	13933 mAh g <sup>-1</sup>	0.40 V	826 h at 1000 mAh g <sup>-1</sup>	[106]
Co <sub>3</sub> O <sub>4</sub>	Co Vacancy	13 331 mAh g <sup>-1</sup>	1.38 V	70 Cycles at 100 mAh g <sup>-1</sup>	[102]
Co <sub>3</sub> O <sub>4</sub>	O Vacancy	24051.2 mAh g <sup>-1</sup>	–	150 cycles At 400 mAh g <sup>-1</sup>	[53]
NiCo <sub>2</sub> O <sub>4</sub>	O Vacancy	8388 mAh g <sup>-1</sup>	–	102 cycles At 340 mAh g <sup>-1</sup>	[107]
Co <sub>3</sub> O <sub>4</sub>	O Vacancy	8250 mAh g <sup>-1</sup>	0.9 V	500 cycles At 100 mAh g <sup>-1</sup>	[108]

efficient heterostructure catalysts by combining spinel with other materials.

Heterostructure engineering can effectively optimize the morphology and structure of the catalysts, which allows more active sites to be exposed and facilitates the diffusion of Li<sup>+</sup> and adsorption of O<sub>2</sub> species, thus accelerating the ORR and OER reaction kinetics. Wu et al. successfully designed a high-quality heterostructure using NiCo<sub>2</sub>O<sub>4</sub> sea urchin-like micro-spheres as the core and CeO<sub>2</sub> nanoparticles as the modifiers in Figure 5a.<sup>[11]</sup> This unique micro-structure with abundant open space and large surface area allows more active sites to be exposed, which contributes to the adsorption of oxygen or lithium ions and the storage of discharge products during the OER/ORR reaction. On the other hand, the introduction of CeO<sub>2</sub> induces the appearance of lattice distortions on NiCo<sub>2</sub>O<sub>4</sub>, contributing to the emergence of more oxygen vacancies and greatly accelerating the charge transfer rate. As shown in the Figure 5b, NiCo<sub>2</sub>O<sub>4</sub>@CeO<sub>2</sub> shows the largest full charge/discharge capacity and the lowest overpotential compared with other single components, fully demonstrating its excellent electrocatalytic performance. DFT calculations were employed to provide insight into the effect of CeO<sub>2</sub> on the catalytic properties of NiCo<sub>2</sub>O<sub>4</sub> at the atomic level. It can be clearly seen in Figure 5c that O<sub>2</sub> and Li start to be adsorbed on the surface of NiCo<sub>2</sub>O<sub>4</sub> and NiCo<sub>2</sub>O<sub>4</sub>@CeO<sub>2</sub> as the ORR reaction proceeds, which further reacts to form LiO<sub>2</sub>. In the subsequent reaction, NiCo<sub>2</sub>O<sub>4</sub>@CeO<sub>2</sub> shows less adsorption to the oxygenated intermediates Li<sub>2</sub>O<sub>2</sub> and Li<sub>3</sub>O<sub>4</sub>, indicating that NiCo<sub>2</sub>O<sub>4</sub>@CeO<sub>2</sub> easily gets covered by Li<sub>2</sub>O<sub>2</sub> aggregates, thus delivering an excellent discharge capacity. On the other hand, the adsorption capacity of Li<sub>2</sub>O and 2(Li<sub>2</sub>O) on the catalyst surface was substantially lower than the adsorption of ORR reaction intermediates, indicating that the discharge reaction proceeded via the 2e<sup>-</sup> pathway. Figure 5c reveals in detail the ORR intermediate product growth paths and corresponding adsorption structures on the NiCo<sub>2</sub>O<sub>4</sub>@CeO<sub>2</sub> surface during the discharge process, which are highly consistent with the above result.

Heterostructure engineering promotes the emergence of built-in electric field, which contributes to accelerating the interfacial charge transfer rate. RuO<sub>2</sub>–Co<sub>3</sub>O<sub>4</sub> heterostructure with abundant oxygen vacancies and large specific surface area was successfully prepared as an efficient electrocatalyst.<sup>[112]</sup> Because of the presence of the built-in electric field, the charge transfer between Co<sub>3</sub>O<sub>4</sub> and RuO<sub>2</sub> at different Fermi energy levels occurs until the charge balance is achieved, thereby effectively modulating the electronic structure of spinel. The electronic structure change can be intuitively observed by X-ray absorption near edge structure analysis of the Co K-edge. As shown in Figure 5e, the absorption edge of RuO<sub>2</sub>–Co<sub>3</sub>O<sub>4</sub> is shifted to a lower energy direction compared with Co<sub>3</sub>O<sub>4</sub>, indicating that Co active site gets electrons and is reduced, and the electronic structure is changed. Furthermore, the coordination of the Co site was analyzed by extended X-ray absorption fine structure in Figure 5f. Apparently, the peak intensity of the Co–O bond in RuO<sub>2</sub>–Co<sub>3</sub>O<sub>4</sub> is weakened, which indicates a decrease in the number of coordination sites in the Co center, verifying the presence of oxygen vacancies. In the Figure 5g, compared with the shorter cycling stability of bulk-phase Co<sub>3</sub>O<sub>4</sub>, the cycling stability of RuO<sub>2</sub>–Co<sub>3</sub>O<sub>4</sub> is significantly improved, fully demonstrating the improved electrocatalytic performance of the spinel material. DFT calculations provide further insight into the intrinsic properties and reactivity of electrocatalysts. As illustrated in Figure 5h, the model structure of RuO<sub>2</sub>–Co<sub>3</sub>O<sub>4</sub> was successfully constructed. It is clearly seen that the presence of a heterogeneous interface causes a change in the coordination structure of spinel material. Moreover, the charge density distribution of the electrocatalyst was further calculated in Figure 5i. There is a significant charge density difference between the RuO<sub>2</sub> and Co<sub>3</sub>O<sub>4</sub> at the two ends of the interface, hence the electronic coupling is stronger in the interface region, which promotes the electron transfer between the components. At last, the free energy diagram in Figure 5j shows that RuO<sub>2</sub>–Co<sub>3</sub>O<sub>4</sub> has a low overpotential ( $\eta = 1.44$  V), which exhibits an excellent electrocatalytic performance, in high agreement with the above results.

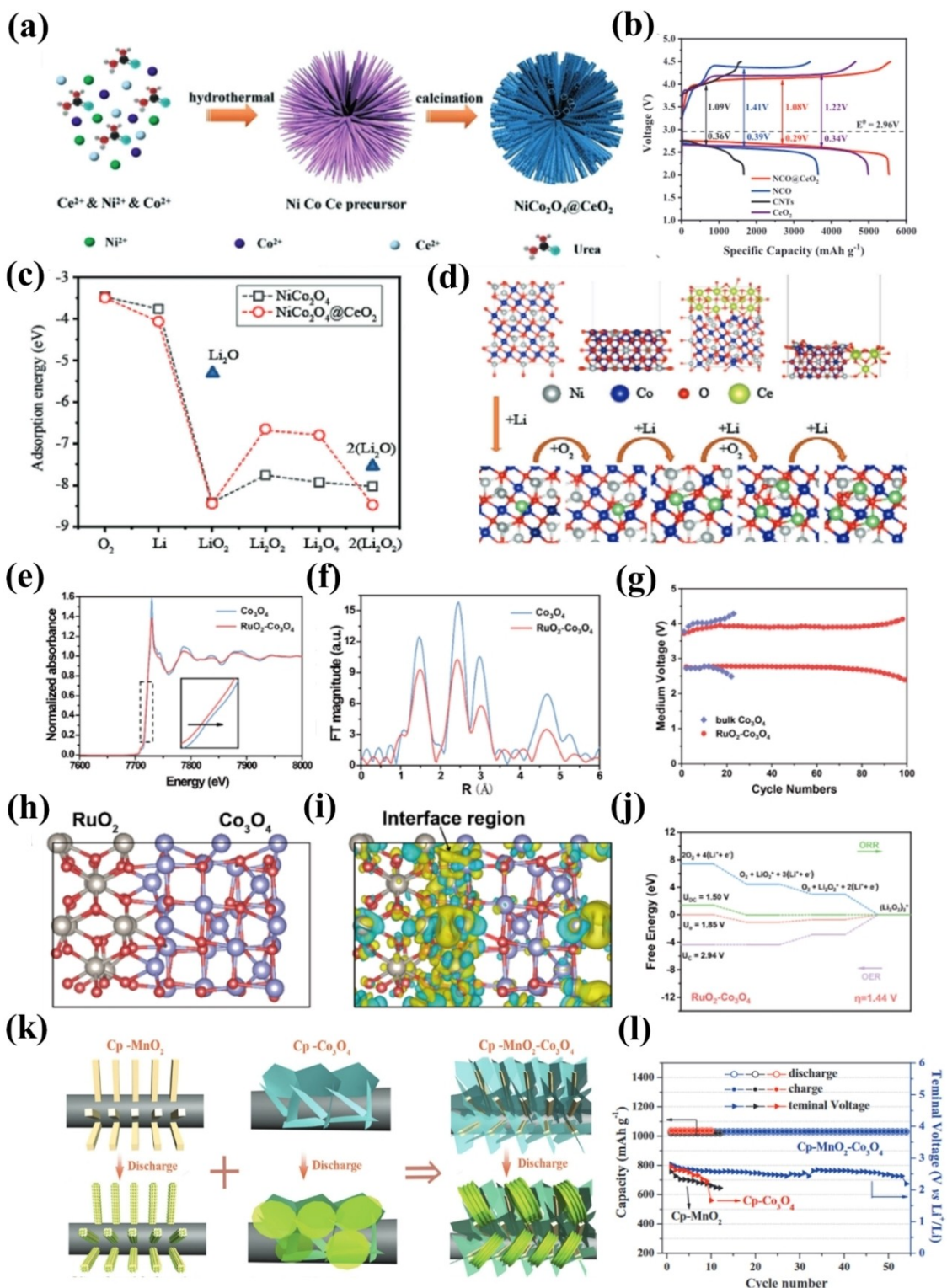


**Figure 5.** (a) The schematic diagram of preparation process for  $\text{NiCo}_2\text{O}_4@\text{CeO}_2$ . (b) The initial discharge/charge curves of  $\text{NiCo}_2\text{O}_4@\text{CeO}_2$ ,  $\text{NiCo}_2\text{O}_4$ ,  $\text{CeO}_2$ , and pure CNTs electrodes. (c) Adsorption energy (Eads) of the ORR intermediates on the  $\text{NiCo}_2\text{O}_4$  surface and  $\text{NiCo}_2\text{O}_4@\text{CeO}_2$  surface. (d) Top and side views of the ORR mechanism for the  $\text{O}_2$  reduction near the  $\text{NiCo}_2\text{O}_4$  or  $\text{NiCo}_2\text{O}_4@\text{CeO}_2$  surface. (e) XANES spectra at the Co K-edge and (f) Fourier transform EXAFS spectrum of  $\text{Co}_3\text{O}_4$  and  $\text{RuO}_2-\text{Co}_3\text{O}_4$ . (g) Cycle number of  $\text{Co}_3\text{O}_4$  and  $\text{RuO}_2-\text{Co}_3\text{O}_4$ . (h) Model structure of the  $\text{RuO}_2-\text{Co}_3\text{O}_4$  interface. (i) Charge-density difference of the  $\text{RuO}_2-\text{Co}_3\text{O}_4$  interface. (j) Free-energy diagrams for ORR/OER catalyzed by  $\text{RuO}_2-\text{Co}_3\text{O}_4$  nanohybrids. (k) Schematic illustration of designing the composite cathode architecture with ideal discharge product morphology based on different discharge characteristics of  $\text{CP}-\text{MnO}_2$  and  $\text{CP}-\text{Co}_3\text{O}_4$ . (l) Cycling performance of the  $\text{CP}-\text{MnO}_2-\text{Co}_3\text{O}_4$ ,  $\text{CP}-\text{MnO}_2$  and  $\text{CP}-\text{Co}_3\text{O}_4$ . (a-d) Reproduced with permission.<sup>[111]</sup> Copyright 2022, Wiley-VCH. (e-j) Reproduced with permission.<sup>[112]</sup> Copyright 2021, American Chemical Society. (k-l) Reproduced with permission.<sup>[113]</sup> Copyright 2017, Wiley-VCH.

Different materials exhibit various electrochemical properties, while heterostructure catalysts provide a synergistic effect by combining the advantages of each material component, hence greatly enhancing the electrocatalytic performance. Zhang's group combined  $\alpha$ -MnO<sub>2</sub> and Co<sub>3</sub>O<sub>4</sub>, both of which exhibit different discharge properties, as cathode catalysts to optimize the growth mechanism of the discharge products, successfully obtaining high-performance LOBs.<sup>[113]</sup> As shown in Figure 5k, the different components of the heterostructure differ in the discharge products formed during the discharge process, in which  $\alpha$ -MnO<sub>2</sub> nanorods adsorb Li<sup>+</sup> and O<sub>2</sub> reduction on the surface through a surface adsorption mechanism, ultimately form homogeneous Li<sub>2</sub>O<sub>2</sub> particles, while Co<sub>3</sub>O<sub>4</sub> nanosheets mainly complete the coupling of O<sub>2</sub><sup>-</sup> and Li<sup>+</sup> in solution through a solvation-mediated mechanism, resulting in the final formation of Li<sub>2</sub>O<sub>2</sub> thin films and Li<sub>2</sub>O<sub>2</sub> nanosheets. Consequently, an excellent synergistic effect occurs when the above two components are combined together in carbon paper to form a CP–MnO<sub>2</sub>–Co<sub>3</sub>O<sub>4</sub> composite electrode:  $\alpha$ -MnO<sub>2</sub> provides the initial nucleation sites for Li<sub>2</sub>O<sub>2</sub>, while Co<sub>3</sub>O<sub>4</sub> nanosheets provide the deposition sites to attract a large amount of dissolved LiO<sub>2</sub>, eventually forming a large-sized and embedded-structured Li<sub>2</sub>O<sub>2</sub> and achieving the enhancement of electrochemical performance for LOBs. The electrochemical experimental results are shown in Figure 5l, compared with the single component, CP–MnO<sub>2</sub>–Co<sub>3</sub>O<sub>4</sub> is able to cycle steadily for nearly 50 times at limited capacity, which significantly improves the performance of LOBs, in line with the expectation of synergistic effect. The electrochemical properties of the related heterostructure-modified spinel in LOBs are shown in Table 3.

#### 4. Spinel Catalytic Activity Descriptors

Over the past decades, many experimental studies have revealed that there is a linear correlation between some surface electronic structures in catalysts and the strength of the catalytic effect, thus they are regarded as catalytic activity

descriptors for screening electrocatalysts with higher activity.<sup>[93,116,117]</sup>

##### 4.1. D-band center

Hammer and Nørskov proposed the d-band theory which enables to describe the relationship between the electronic structure of transition metal atoms and catalytic activity.<sup>[118]</sup> Specifically, when a reactant adsorbs on a TM surface, the valence state first couples to the TM s state, the corresponding valence state broadens and moves downward, and then interacts with the TM d state to form bonding orbitals and partially occupied antibonding orbitals. It is worth noting that when the filling of antibonding orbitals increases, the adsorption of reactants is weaker, while the filling of antibonding orbitals decreases, the adsorption of reactants is stronger, accordingly, the position of the d-band center can be regulated to reactants bonding. In summary, the closer the d-band center is to the Fermi energy level (E<sub>f</sub>), the fewer the electrons in the antibonding orbitals are, the stronger the ability to adsorb the reactants, and conversely, the weaker it is.

The d-band theory clearly reveals the bonding rules between TMs and reactants, reflects the variation trend of catalytic activity, providing a direction for the construction of high-activity electrocatalysts. Qu et al. optimized the electronic structure of Co<sub>3</sub>O<sub>4</sub> spinel by different cation substitutions, thus selecting spinel materials with high catalytic activity.<sup>[119]</sup> As seen in Figure 6a, the density of states (DOS) of the spinel materials is clearly observed, three samples possess a high DOS at E<sub>f</sub>, which show strong metallicity, suggesting a fast electron transfer in MCo<sub>2</sub>O<sub>4</sub> (M=Co, Ni, Mg). Then, the Co 3d partial wave density of states (PDOS) is further investigated in Figure 6b. Notably, it can be found that the center of the Co d-band shifts towards E<sub>f</sub> when Ni and Mg replace the Co sites, revealing a change in the electronic structure. Based on the d-band theory, the interaction of MCo<sub>2</sub>O<sub>4</sub> with reactants leads to corresponding bonding and antibonding orbitals in Figure 6c.

**Table 3.** Electrochemistry performance of recently reported common spinels with heterostructure modifications in LOBs.

Electrocatalysts	Modification strategies	Specific capacity	Overpotential	Cycle ability	Ref.
NiCo <sub>2</sub> O <sub>4</sub>	Heterostructure (CeO <sub>2</sub> )	5537.0 mAh g <sup>-1</sup>	1.07 V	400 cycles At 500 mA g <sup>-1</sup>	[111]
Co <sub>3</sub> O <sub>4</sub>	Heterostructure (RuO <sub>2</sub> )	19747.0 mAh g <sup>-1</sup>	–	100 cycles At 200 mA g <sup>-1</sup>	[112]
Co <sub>3</sub> O <sub>4</sub>	Heterostructure (NiCo <sub>2</sub> O <sub>4</sub> )	11672.8 mAh g <sup>-1</sup>	1.01 V	280 cycles At 600 mA g <sup>-1</sup>	[114]
Co <sub>3</sub> O <sub>4</sub>	Heterostructure (CeO <sub>2</sub> @Co/N–CNF)	9667.3 mAh g <sup>-1</sup>	0.87 V	70 cycles At 100 mA g <sup>-1</sup>	[115]
NiFe <sub>2</sub> O <sub>4</sub>	Heterostructure (MoS <sub>2</sub> )	21526.0 mAh g <sup>-1</sup>	1.0 V	268 cycles At 200 mA g <sup>-1</sup>	[54]

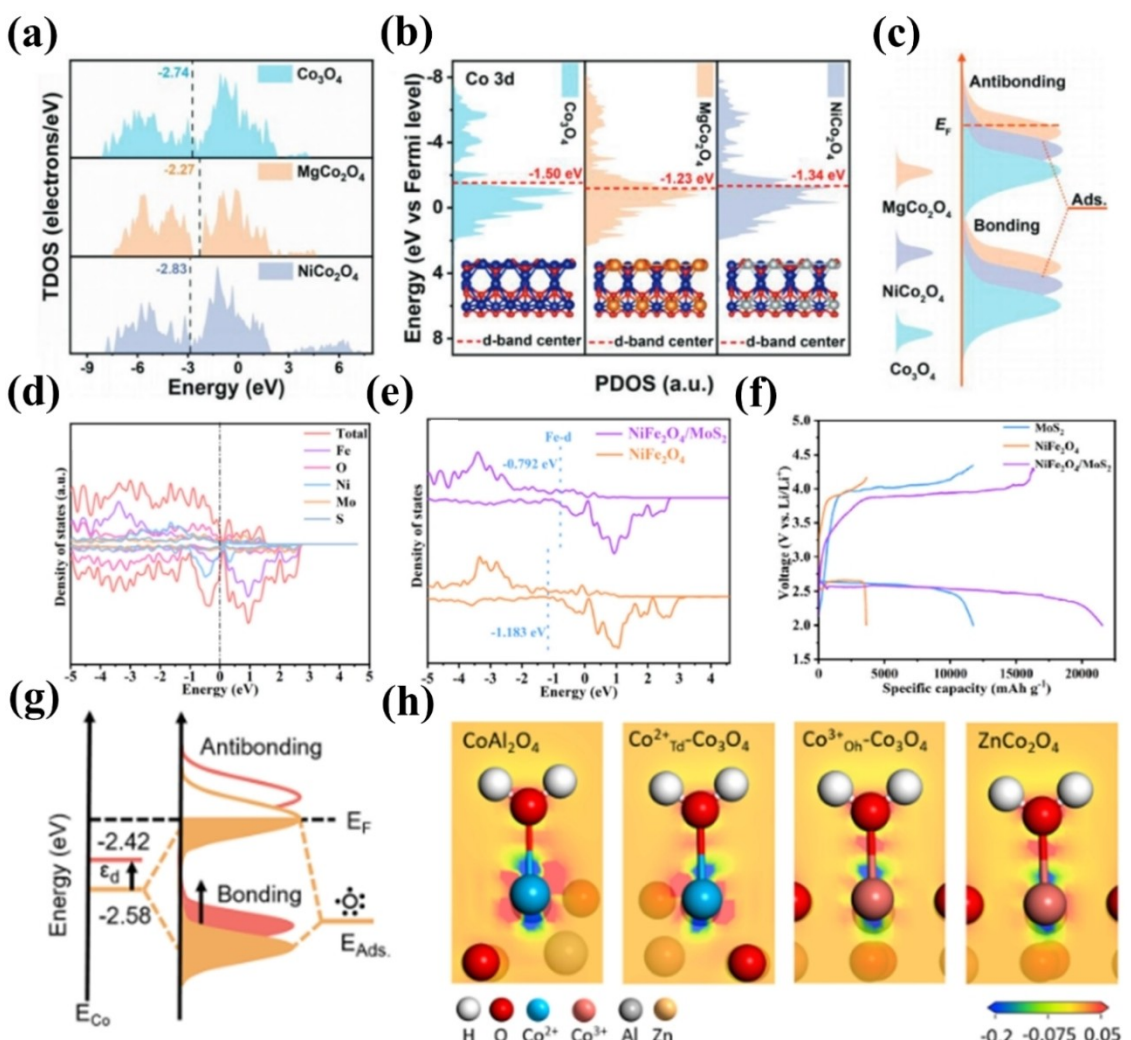


**Figure 6.** (a) Density of states (DOS) and (b) d-band centers of  $\text{Co}_3\text{O}_4$ ,  $\text{MgCo}_2\text{O}_4$ , and  $\text{NiCo}_2\text{O}_4$ . (c) Schematic illustration of bond formation between the catalyst surface and the adsorbates (Ads.). (d) DOS curves of the  $\text{NiFe}_2\text{O}_4/\text{MoS}_2$ . (e) The diagram of d-band center of Fe for  $\text{NiFe}_2\text{O}_4$  and  $\text{NiFe}_2\text{O}_4/\text{MoS}_2$ . (f) The initial discharge/charge profiles of  $\text{NiFe}_2\text{O}_4$ ,  $\text{MoS}_2$  and  $\text{NiFe}_2\text{O}_4/\text{MoS}_2$ . (g) Schematic bond formation between the  $\text{Co}_{\text{oh}}^{3+}$  and  $\text{Co}_{\text{td}}^{2+}$  sites on the  $\text{Co}_3\text{O}_4$  surface and the reactants. (h) Electron density difference diagram of reactants adsorption at the Co site on various catalyst surfaces. (a–c) Reproduced with permission.<sup>[119]</sup> Copyright 2023, Wiley-VCH. (d–f) Reproduced with permission.<sup>[54]</sup> Copyright 2022, Elsevier. (g–h) Reproduced with permission.<sup>[120]</sup> Copyright 2022, American Chemical Society.

Among them, the d energy level of  $\text{Co}_3\text{O}_4$  shifted upward after cation substitution, the high-energy antibonding orbitals likewise shifted upward, which causes the electrons became less occupied, leading to the enhancement of oxygen-containing reactant interactions on the surface of  $\text{MCo}_2\text{O}_4$ , finally accelerating the corresponding reaction kinetics. Apart from cation substitution,  $\text{NiFe}_2\text{O}_4$  spinel was similarly optimized for Fe d-band level by heterostructure engineering.<sup>[54]</sup> Firstly,  $\text{NiFe}_2\text{O}_4/\text{MoS}_2$  exhibits high electrical conductivity with high DOS at  $E_f$  in Figure 6d. Moreover, the PDOS of Fe sites was further obtained in Figure 6e. The d-band center corresponding to the Fe sites of  $\text{NiFe}_2\text{O}_4/\text{MoS}_2$  are closer to  $E_f$ , indicating that the binding of Fe sites to oxygen-containing intermediates becomes stronger, which promotes the growth of  $\text{Li}_2\text{O}_2$  on the catalyst surface via the surface adsorption mechanism and enhances the electrochemical performance of LOBs. As expected,  $\text{NiFe}_2\text{O}_4/\text{MoS}_2$

exhibits the largest charge/discharge capacity in the Figure 6f, demonstrating the excellent electrocatalytic activity.

A noteworthy point is that the d-band level of the active sites in different geometrical configurations in the spinel material can differ in electrocatalytic activity. Wu's group replaced Co tetrahedral ( $\text{Co}_{\text{td}}^{2+}$ ) and Co octahedral ( $\text{Co}_{\text{oh}}^{3+}$ ) in  $\text{Co}_3\text{O}_4$  with  $\text{Zn}^{2+}$  and  $\text{Al}^{3+}$  to form  $\text{ZnCo}_2\text{O}_4$  and  $\text{Co Al}_2\text{O}_4$ , respectively, resulting in a single Co-site active conformation.<sup>[120]</sup> As shown in the Figure 6g, the reactants are adsorbed on the  $\text{Co}_{\text{oh}}^{3+}$  and  $\text{Co}_{\text{td}}^{2+}$  sites on the  $\text{Co}_3\text{O}_4$  surface, respectively, where the d-band center of the  $\text{Co}_{\text{oh}}^{3+}$  is significantly higher than that of  $\text{Co}_{\text{td}}^{2+}$ . Among them, due to the antibonding orbital of  $\text{Co}_{\text{oh}}^{3+}$  is higher than that of  $\text{Co}_{\text{td}}^{2+}$ , the corresponding electron occupation is less, which enhances the interaction between  $\text{Co}_{\text{oh}}^{3+}$  and the reactants, promoting the electron transfer and improving the electrocatalytic performance. The blue area represents the electron loss when the cobalt sites

adsorb the reactants, while the red area signifies the electron gain in Figure 6h. Compared to the  $\text{Co}_{\text{Td}}^{2+}$  sites, the electrons on the  $\text{Co}_{\text{Oh}}^{3+}$  sites are more easily transferred to the O atoms of the reactants, suggesting a stronger adsorption to the reactants, in agreement with the above finding.

#### 4.2. $e_g$ occupancy

Shao Horn et al. were one of the earliest to discover in perovskites that the  $e_g$  occupancy of octahedral cations is closely related to the capacity of the catalyst to adsorb reactants.<sup>[121]</sup> Similarly, the same phenomenon exists in other transition metal oxides, hence  $e_g$  occupation can function as a catalytic descriptor for spinel oxides to regulate reactant-catalyst adsorption bonding. As is known, in spinel, when the metal sites form on an octahedral coordination structure, the corresponding d orbital splits into two pairs of orbitals,  $t_{2g}$  and

$e_g$ , among which the  $e_g$  orbitals are at the higher energy level and the  $t_{2g}$  orbitals are at the lower energy level. The  $e_g$  orbitals strongly overlap with the O 2p orbitals, forming  $\sigma$  and  $\sigma^*$  bond states. Whereas the  $t_{2g}$  orbitals show a weaker overlap with the O 2p orbitals, forming  $\pi$  and  $\pi^*$  bond states. In this case, the adsorption of the catalyst towards the reactants is mainly determined by the  $\sigma$  interactions of the  $e_g$  states, thus the mutual bonding between the reactants and the catalyst surface is modulated by the electron occupation of the  $e_g$  orbitals.

The  $e_g$  occupation descriptor effectively describes the interaction between reactants and catalysts, contributing to the design and preparation of efficient catalysts. As shown in Figure 7a, with the gradual increase of  $e_g$  orbital occupation, the spin state of  $\text{ZnCo}_2\text{O}_4$  spinel (ZCO) changes (low spin to high spin), which enhances the adsorption of reactants, showing good catalytic performance.<sup>[122]</sup> In addition, the spin state distribution of ZCO was further calculated in Figure 7b. It is found that the proportion of HS  $\text{Co}^{3+}$  in ZCO gradually

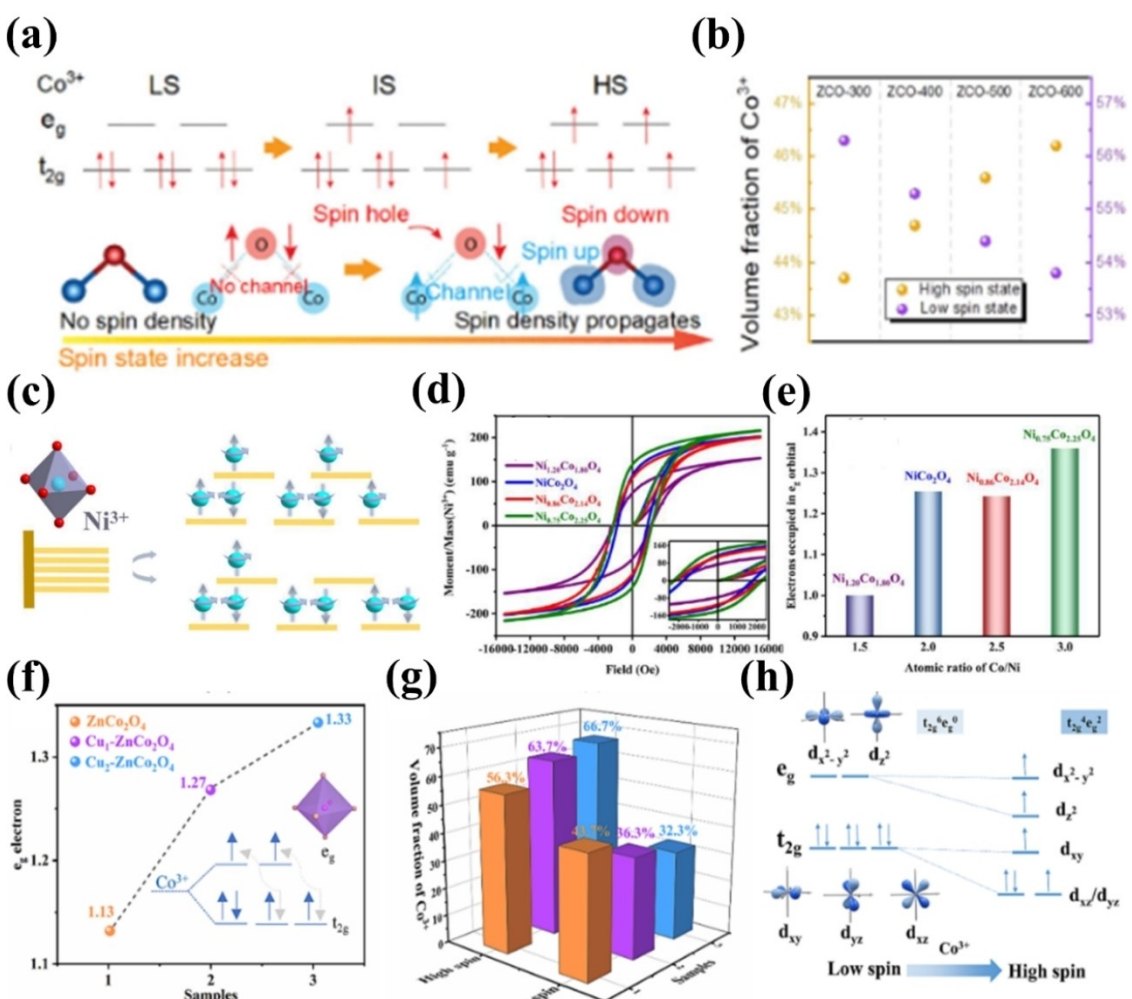


**Figure 7.** (a) Illustration of the evolution of  $\text{Co}^{3+}$  spin state and Co–O–Co spin channel during the process of raising the cobalt spin state. (b) The calculated volume fraction of HS and LS state  $\text{Co}^{3+}$  in the four  $\text{ZnCo}_2\text{O}_4$  samples. (c) Spin states of  $\text{Ni}^{3+}$  at octahedral sites in  $\text{Ni}_x\text{Co}_{3-x}\text{O}_4$ . (d) Magnetic characterization of  $\text{Ni}_x\text{Co}_{3-x}\text{O}_4$  ( $x = 0, 0.75, 0.86, 1$ , and  $1.20$ ) obtained at 2 K. (e) Electron occupation in the  $e_g$  orbital of  $\text{Ni}_x\text{Co}_{3-x}\text{O}_4$ . (f) The corresponding  $e_g$  occupation of  $\text{ZnCo}_2\text{O}_4$ ,  $\text{Cu}_1\text{-ZnCo}_2\text{O}_4$  and  $\text{Cu}_2\text{-ZnCo}_2\text{O}_4$ . (g) The calculated volume fraction of high spin and low spin state  $\text{Co}^{3+}$  for three samples. (h) Schematic configurations for high spin and low spin states of  $\text{Co}^{3+}$ . (a–b) Reproduced with permission.<sup>[122]</sup> Copyright 2021, Wiley-VCH. (c–e) Reproduced with permission.<sup>[123]</sup> Copyright 2021, American Chemical Society. (f–h) Reproduced with permission.<sup>[97]</sup> Copyright 2023, Elsevier.

increases with increasing temperature, hence ZCO-600 has higher  $e_g$  occupancy, showing excellent electrocatalytic performance. Of note,  $\text{NiCo}_2\text{O}_4$  spinel displaces some of the  $\text{Co}^{3+}$  octahedra by varying the Ni elemental content, where electrons leap from  $t_{2g}$  into  $e_g$ , optimizing  $e_g$  orbital occupancy (Figure 7c).<sup>[123]</sup> By saturation magnetization curves of samples at 2 K in Figure 7d. The variation of the ferromagnetism of inverse spinel  $\text{Ni}_x\text{Co}_{3-x}\text{O}_4$  is closely correlated with the  $\text{Ni}^{3+}$  replacing the octahedral positions. Further specific  $e_g$  orbital occupancies of  $\text{Ni}_x\text{Co}_{3-x}\text{O}_4$  were derived by calculations in Figure 7e. Compared to other contents of  $\text{Ni}_x\text{Co}_{3-x}\text{O}_4$  with  $e_g$  occupancy larger than 1, it is found that  $e_g$  occupancy close to 1 in  $\text{Ni}_{1.20}\text{Co}_{1.80}\text{O}_4$  display better catalytic properties, thereby accelerating reaction kinetics. Aside from directly altering the electrochemical ratios of spinel,  $\text{ZnCo}_2\text{O}_4$  spinel also achieves a change in the Co octahedral coordination structure through the introduction of foreign inert Cu ions, which in turn modulates  $e_g$  orbital occupancy, greatly enhancing the electrochemical performance of LOBs.<sup>[97]</sup> As shown in Figure 7f, it is obvious that  $\text{Cu}_{1-x}\text{ZnCo}_2\text{O}_4$  has a moderate  $e_g$  occupancy, which is not too strong and not too weak for the adsorption of the reaction intermediates, in favor of accelerating the OER/ORR reaction kinetics. Figure 7g reveals the increase in the high spin  $\text{Co}^{3+}$  volume fraction in  $\text{ZnCo}_2\text{O}_4$  with the introduction of Cu. During the process of spin state raising, the specific changes in the electronic structure are shown in Figure 7h, the electrons jump from the  $d_{xz}$  and  $d_{yz}$  orbitals to the  $d_{z^2}$  and  $d_{x^2-y^2}$  empty orbitals, which optimizes the  $e_g$  orbital occupancy, effectively improving the electrocatalytic activity of  $\text{ZnCo}_2\text{O}_4$ .

### 4.3. Metal–O covalency

As well as the proposal of  $e_g$  occupation descriptors, Shao-Horn group has also identified metal–O (M–O) covalency as a valid descriptor of catalytic activity, which is attributed to the ionic-covalent mixing properties of the metal–oxygen bonding of the oxides (energetic similarity (covalency) and spatial overlap (hybridization) of the metal 3d orbitals and the O 2p states) in correlation with the catalytic activity.<sup>[124]</sup> Notably, Sun et al. state that M–O covalency can be quantified by the distance between the centers of the metal d band and O p band (charge transfer energy), with larger distances indicating weaker M–O covalency and vice versa.<sup>[125]</sup> In spinel electrocatalysts, the strong M–O covalency suggests that the active redox couple of octahedral metal sites display stronger O 2p characteristics, which facilitates the charge transfer between the active sites and oxygen-containing intermediates. Also note that even though the movement of the O p-band center towards  $E_f$  promotes OER activity, moving too close to  $E_f$  rather decreases the stability of the catalysts, adversely affecting the electrochemical reaction.

The oxygen vacancy formation energy, oxygen binding energy and electron transfer barrier related to the catalysts can be predicted from the M–O covalency, which are useful for screening and constructing catalysts with high catalytic activity. As shown in Figure 8a, the intensity of the O K-edge peak representing the electronic excitation of the O 1s nucleus

increases, which fully illustrates that filling the oxygen vacancy-rich  $\text{ZnCo}_2\text{O}_4$  with F enhances the covalence of the Co–O bond, boosting the electrocatalytic activity.<sup>[126]</sup> It is evident from Figure 8b that the F anion promotes the activation of lattice oxygen, which shifts the O 2p band towards the Fermi energy level, enhancing the hybridization between Co 3d and O 2p. At the same time, the d-band center of Co 3d is also shifted upwards, which suggests that Co has a stronger ability to get electron, accelerating the electron transfer between Co and the intermediate and improving the electrocatalytic performance. Furthermore, Ni doping  $\text{ZnCo}_2\text{O}_4$  effectively changes the DOS distribution of catalyst in Figure 8c.<sup>[52]</sup> The emergence of non-bonded oxygen p states on spinel  $\text{ZnNi}_{0.8}\text{Co}_{1.2}\text{O}_4$  with the increase of Ni content fully illustrates the change of the relative positions of both the metal d-band center and the O p-band center. Specifically, the d-band center of Ni poor spinel is at a higher position than the O p-band center, showing greater metallic properties. In contrast, the O p band center of the Ni rich spinel is located at a higher position than the d band center, which displays a stronger M–O covalency, thus facilitating electron transfer and greatly enhancing the catalytic activity (Figure 8d). Remarkably, the relationship between the OER activity of Fe doping  $\text{ZnCo}_2\text{O}_4$  spinel and Co–O covalency is further explored via the N–V parameter (N is the number of unpaired electrons of Co atoms, and V is the nominal valence of Co cations) in Figure 8e.<sup>[127]</sup> N–V represents the net ability of the octahedral sites to provide electrons. When the ability of Co sites to provide electrons to oxygen is lower, it is easy to achieve the drag-off of the electron density of the oxygen atom, which leads to the enhancement of Co–O covalency and optimization of the OER activity. As a result,  $\text{ZnFe}_{0.4}\text{Co}_{1.6}\text{O}_4$  with the smallest N–V value exhibits the strongest Co–O covalency, showing excellent catalytic activity. The above results can be further verified by DOS calculations in Figure 8f. It is obvious that the Co 3d center and O 2p center in  $\text{Zn}_{1-x}\text{Fe}_x\text{ZnCo}_2\text{O}_4$  are not far away from each other, which exhibits excellent Co–O covalency and contributes to the electron transfer between Co sites and oxygenated intermediates, greatly accelerating the OER reaction kinetics.

## 5. Conclusion and Perspectives

One of the most promising research directions to advance the electrochemical performance of LOBs is the exploitation of efficient and low-cost cathode catalysts. A premise for the rational design of efficient catalysts is an in-depth insight into the ORR and OER mechanisms in LOBs. In this review, we have summarized the advantages of spinel-type catalysts for LOBs, including their unique coordination structure, easily exposed active sites, and low cost, along with the corresponding modification strategies. Furthermore, we have explored the correlation between spinel catalysts and their catalytic behaviors, providing a feasible reference for the design and preparation of efficient catalysts. Despite the significant progress made by spinel-type catalysts in improving the electrochemical performance of LOBs, there is ample room for

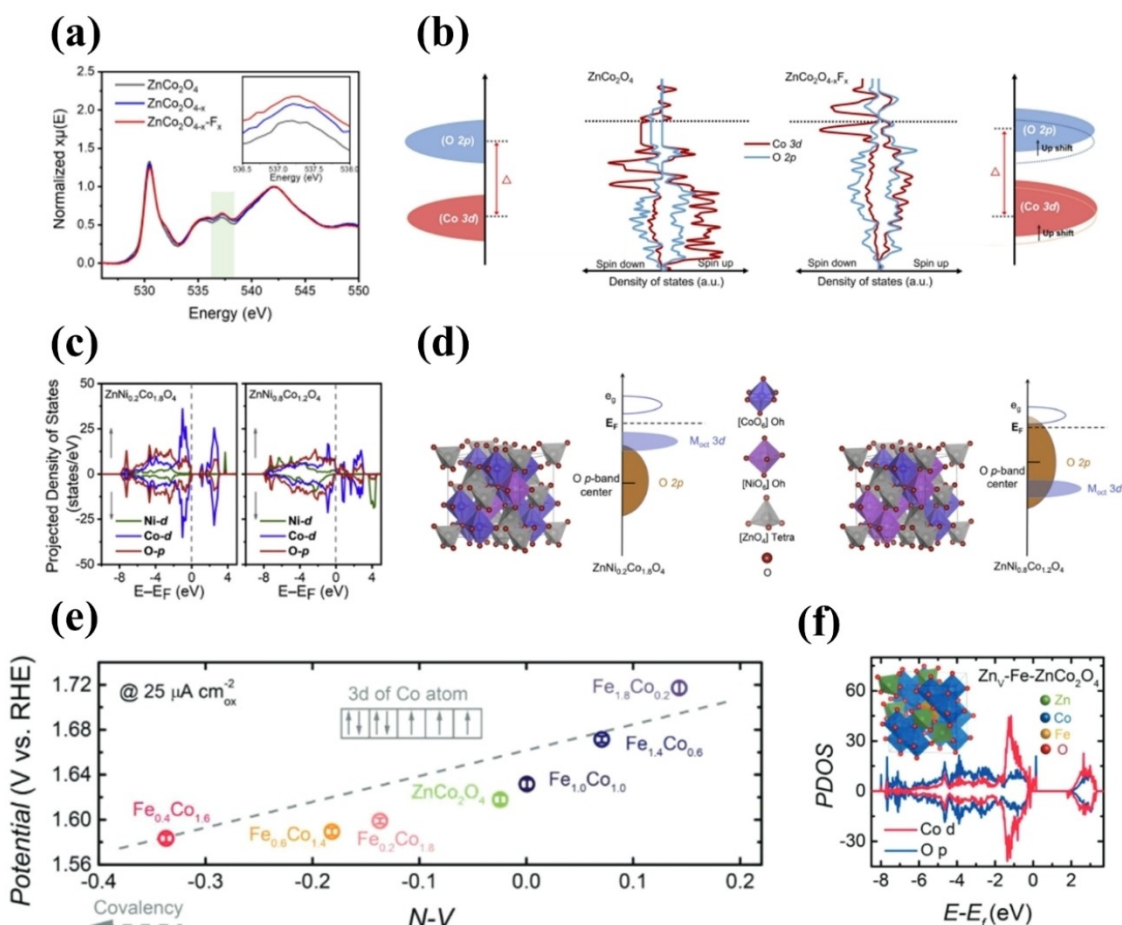


**Figure 8.** (a) O K-edge XANES spectra of ZnCo<sub>2</sub>O<sub>4</sub>, ZnCo<sub>2</sub>O<sub>4-x</sub> and ZnCo<sub>2</sub>O<sub>4-x</sub>F<sub>x</sub>. (b) the schematic band diagrams and density of states of ZnCo<sub>2</sub>O<sub>4</sub> and ZnCo<sub>2</sub>O<sub>4-x</sub>F<sub>x</sub>. (c) PDOS of the O p states and metal d states in ZnNi<sub>0.2</sub>Co<sub>1.8</sub>O<sub>4</sub> and ZnNi<sub>0.8</sub>Co<sub>1.2</sub>O. (d) Spinel structures and schematic representation of the O p-band center and metal d-band center for ZnNi<sub>0.2</sub>Co<sub>1.8</sub>O<sub>4</sub> and ZnNi<sub>0.8</sub>Co<sub>1.2</sub>O. (e) The OER activity as a function of the N-V parameter for Fe doping ZnCo<sub>2</sub>O<sub>4</sub>. (f) PDOS of Zn<sub>V</sub>-Fe-ZnCo<sub>2</sub>O<sub>4</sub>. (a–b) Reproduced with permission.<sup>[126]</sup> Copyright 2023, Wiley-VCH. (c–d) Reproduced with permission.<sup>[52]</sup> Copyright 2019, Elsevier. (e–f) Reproduced with permission.<sup>[127]</sup> Copyright 2018, Wiley-VCH.

exploration and many challenges in practical applications. More progress is available to build on the following aspects.

(1) **Enhancing the pristine catalytic performance of spinel.** The pristine catalytic performance of spinel is determined by both the intrinsic catalytic activity of the metal active sites and the number of active sites. Accordingly, in an attempt to obtain high catalytic activity, spinel catalysts need to be designed and prepared from the above two aspects. On the one hand, the A-, B- and O-sites of spinel are occupied by many different cations or anions, exhibiting diverse intrinsic catalytic activities. Given the variety of elemental combinations, screening and synthesizing catalysts with high catalytic activity spinel generally requires a great deal of time. As a result, extensive basic data from machine learning and calculation simulation can be obtained, and it is further analyzed to screen catalysts with high intrinsic activity, which provides data support for the design of ideal spinel. On the other hand, the design of suitable spinel morphology structure with high specific surface area and controllable porosity, which exposes enough active sites, greatly enhancing the catalytic performance. Therefore,

there exists a sufficient contact area at the triple boundary of oxygen, electrolyte and oxygen electrode in LOBs, which contributes to accelerated charge transfer and Li<sup>+</sup> transport on the one hand, and promotes reversible formation and decomposition of discharge products on the other hand.

(2) **In-depth analysis of the catalyst mechanism in conjunction with in-situ technologies.** It is well known that the characterization of cathode catalysts in LOBs is mostly performed before or after electrochemical tests, which results in the difficulty of detecting the evolution of oxygen-containing intermediates and their adsorption on the catalyst surface, preventing in-depth study of the ORR/OER reaction mechanism. In situ technology not only effectively monitors the catalyst surface changes but also tracks the evolution of oxygen-containing intermediates in a timely manner, which facilitates the elucidation of the specific working principle of spinel catalysts in LOBs. In situ Raman spectroscopy allows the observation of changes over time in the species and content of discharge products on the surface of spinel catalysts in LOBs. In situ IR spectroscopy tracks the evolution of oxygen-containing

intermediates in LOBs and the actual adsorption state. In situ DEMS discerns the specific reaction pathways of discharge product generation by analyzing the gas consumption and emission during the charging and discharging of LOBs. As mentioned above, in situ technology contributes to the determination of the catalytic role of spinel catalysts in LOBs, which enables the construction of realistic and credible theoretical computational models for an in-depth analysis of the ORR/OER reaction mechanism.

(3) **Further exploration of universal catalytic descriptors.** Catalytic descriptors clearly elucidate the correlation between the electronic structure and catalytic activity of spinel, on the basis of which the subsequent catalytic activity trends are accurately predicted, which is conducive to the design of spinel catalysts with high catalytic performance. Nevertheless, there are always some limitations of a single descriptor in describing the electronic structure-catalytic activity relationship. For example, the  $e_g$  occupation on the ionic model often fails to cover metal–oxygen covalency effectively. Additionally, there are differences in the surface and bulk electronic structures of the catalysts, and the corresponding correlation with the catalytic activity varies. In conclusion, it is very feasible to combine multiple descriptors and apply them together to predict the catalytic activity variation. Notably, the catalytic reaction mainly occurs on the catalyst surface, thus the coordination environment of the catalyst and the information of the surface electronic structure need to be adequately taken into account when constructing the descriptor. Consequently, achieving the goal of elucidating the relationship between catalyst electronic structure and catalytic activity by using one rational and effective catalytic descriptor still requires considerably more research.

## Acknowledgements

The authors acknowledge the financial support provided by the National Natural Science Foundation of China (21805018; 52002039) and Natural Science Foundation of Sichuan Province (2023NSFSC1079).

## Conflict of Interests

The authors declare no competing financial interest.

**Keywords:** Lithium–oxygen batteries · spinel-type electrocatalysts · modification strategies · catalytic descriptor

- [1] S. Ahn, C. Zor, S. Yang, M. Lagnoni, D. Dewar, T. Nimmo, C. Chau, M. Jenkins, A. J. Kibler, A. Pateman, G. J. Rees, X. Gao, P. Adamson, N. Grobert, A. Bertei, L. R. Johnson, P. G. Bruce, *Nat. Chem.* **2023**, *15*, 1022.
- [2] A. Kondori, M. Esmaeilirad, A. M. Harzandi, R. Amine, M. T. Saray, L. Yu, T. Liu, J. Wen, N. Shan, H.-H. Wang, A. T. Ngo, P. C. Redfern, C. S. Johnson, K. Amine, R. Shahbazian-Yassar, L. A. Curtiss, M. Asadi, *Science* **2023**, *379*, 499.

- [3] C. Zhao, Z. Yan, B. Zhou, Y. Pan, A. Hu, M. He, J. Liu, J. Long, *Angew. Chem. Int. Ed.* **2023**, *62*, e202302746.
- [4] G. Zheng, T. Yan, Y. Hong, X. Zhang, J. Wu, Z. Liang, Z. Cui, L. Du, H. Song, *Nat. Commun.* **2023**, *14*, 2268.
- [5] A. Hu, W. Chen, F. Li, M. He, D. Chen, Y. Li, J. Zhu, Y. Yan, J. Long, Y. Hu, T. Lei, B. Li, X. Wang, J. Xiong, *Adv. Mater.* **2023**, *35*, 2304762.
- [6] A. Hu, W. Chen, X. Du, Y. Hu, T. Lei, H. Wang, L. Xue, Y. Li, H. Sun, Y. Yan, J. Long, C. Shu, J. Zhu, B. Li, X. Wang, J. Xiong, *Energy Environ. Sci.* **2021**, *14*, 4115.
- [7] Z. Chang, J. Xu, X. Zhang, *Adv. Energy Mater.* **2017**, *7*, 1700875.
- [8] B. He, G. Li, J. Li, J. Wang, H. Tong, Y. Fan, W. Wang, S. Sun, F. Dang, *Adv. Energy Mater.* **2021**, *11*, 2003263.
- [9] L.-N. Song, W. Zhang, Y. Wang, X. Ge, L.-C. Zou, H.-F. Wang, X.-X. Wang, Q.-C. Liu, F. Li, J.-J. Xu, *Nat. Commun.* **2020**, *11*, 2191.
- [10] W. Yao, Y. Yuan, G. Tan, C. Liu, M. Cheng, V. Yurkiv, X. Bi, F. Long, C. R. Friedrich, F. Mashayek, K. Amine, J. Lu, R. Shahbazian-Yassar, *J. Am. Chem. Soc.* **2019**, *141*, 12832.
- [11] J.-J. Xu, Z.-W. Chang, Y. Wang, D.-P. Liu, Y. Zhang, X.-B. Zhang, *Adv. Mater.* **2016**, *28*, 9620.
- [12] J. Lee, T. H. Lee, H. W. Jang, H. S. Park, *InfoMat* **2022**, *4*, e12268.
- [13] Q. Han, W. Guo, X. He, T. Liu, X. Liu, X. Zhu, T. Bian, L. Jiang, J. Lu, Y. Zhao, *Joule* **2022**, *6*, 381.
- [14] T. Bai, D. Li, S. Xiao, F. Ji, S. Zhang, C. Wang, J. Lu, Q. Gao, L. Ci, *Energy Environ. Sci.* **2023**, *16*, 1431.
- [15] Z. Sun, X. Zhao, W. Qiu, B. Sun, F. Bai, J. Liu, T. Zhang, *Adv. Mater.* **2023**, *35*, 210867.
- [16] Z. Liu, Z. Zhao, W. Zhang, Y. Huang, Y. Liu, D. Wu, L. Wang, S. Chou, *InfoMat* **2022**, *4*, e12260.
- [17] C. Xu, A. Ge, K. Kannari, B. Peng, M. Xue, B. Ding, K. Inoue, X. Zhang, S. Ye, *ACS Energy Lett.* **2023**, *8*, 1289.
- [18] D. Li, L. Zhao, Q. Xia, J. Wang, X. Liu, H. Xu, S. Chou, *Adv. Funct. Mater.* **2022**, *32*, 2108153.
- [19] J. Zhang, B. Sun, Y. Zhao, A. Tkacheva, Z. Liu, K. Yan, X. Guo, A. M. McDonagh, D. Shanmukaraj, C. Wang, T. Rojo, M. Armand, Z. Peng, G. Wang, *Nat. Commun.* **2019**, *10*, 602.
- [20] Q. Lv, Z. Zhu, S. Zhao, L. Wang, Q. Zhao, F. Li, L. A. Archer, J. Chen, *J. Am. Chem. Soc.* **2021**, *143*, 1941.
- [21] Z. Xie, Z. Lu, J. Wang, Y. Qu, L. Duan, *ACS Sustainable Chem. Eng.* **2023**, *11*, 6698.
- [22] X. Zheng, M. Yuan, D. Guo, C. Wen, X. Li, X. Huang, H. Li, G. Sun, *ACS Nano* **2022**, *16*, 4487.
- [23] H. Xia, Q. Xie, Y. Tian, Q. Chen, M. Wen, J. Zhang, Y. Wang, Y. Tang, S. Zhang, *Nano Energy* **2021**, *84*, 105877.
- [24] D. Chen, R. Yu, R. Lu, Z. Pu, P. Wang, J. Zhu, P. Ji, D. Wu, J. Wu, Y. Zhao, Z. Kou, J. Yu, S. Mu, *InfoMat* **2022**, *4*, e12287.
- [25] C. Ye, M. Zheng, Z. Li, Q. Fan, H. Ma, X. Fu, D. Wang, J. Wang, Y. Li, *Angew. Chem. Int. Ed.* **2022**, *61*, e202213366.
- [26] K. Du, L. Zhang, J. Shan, J. Guo, J. Mao, C.-C. Yang, C.-H. Wang, Z. Hu, T. Ling, *Nat. Commun.* **2022**, *13*, 5448.
- [27] Y. Zhou, Q. Gu, K. Yin, Y. Li, L. Tao, H. Tan, Y. Yang, S. Guo, *Angew. Chem. Int. Ed.* **2022**, *61*, e202201416.
- [28] K. Song, J. Jung, M. Park, H. Park, H.-J. Kim, S.-I. Choi, J. Yang, K. Kang, Y.-K. Han, Y.-M. Kang, *ACS Catal.* **2018**, *8*, 9006.
- [29] X. Zhang, W. Zhang, J. Dai, M. Sun, J. Zhao, L. Ji, L. Chen, F. Zeng, F. Yang, B. Huang, L. Dai, *InfoMat* **2022**, *4*, e12273.
- [30] Y. Gao, S. Liang, B. Liu, C. Jiang, C. Xu, X. Zhang, P. Liang, M. Elimelech, X. Huang, *Nat. Commun.* **2023**, *14*, 2059.
- [31] Y. Yang, L. Zhang, Z. Hu, Y. Zheng, C. Tang, P. Chen, R. Wang, K. Qiu, J. Mao, T. Ling, S. Qiao, *Angew. Chem. Int. Ed.* **2020**, *59*, 4525.
- [32] J. Hu, C. Su, R. Li, B. Li, Z. Hou, Y. Fan, Y. Pan, J. Liu, A. Hu, *J. Alloys Compd.* **2024**, *976*, 173146.
- [33] X. Cao, X. Zheng, Z. Sun, C. Jin, J. Tian, S. Sun, R. Yang, *Appl. Catal. B* **2019**, *253*, 317.
- [34] H. Huang, C. Cheng, G. Zhang, L. Guo, G. Li, M. Pan, F. Dang, X. Mai, *Adv. Funct. Mater.* **2022**, *32*, 2111546.
- [35] S. Jing, Y. Zhang, F. Chen, H. Liang, S. Yin, P. Tsakaras, *Appl. Catal. B* **2019**, *245*, 721.
- [36] K. Wang, Y. Guo, Z. Chen, D. Wu, S. Zhang, B. Yang, J. Zhang, *InfoMat* **2022**, *4*, e12251.
- [37] C. Zhang, M.-Y. Li, J. Tersoff, Y. Han, Y. Su, L.-J. Li, D. A. Muller, C.-K. Shih, *Nat. Nanotechnol.* **2018**, *13*, 152.
- [38] W. Zhong, Z. Wang, N. Gao, L. Huang, Z. Lin, Y. Liu, F. Meng, J. Deng, S. Jin, Q. Zhang, L. Gu, *Angew. Chem. Int. Ed.* **2020**, *59*, 22743.
- [39] Y. Huang, S. L. Zhang, X. F. Lu, Z. Wu, D. Luan, X. W. (David) Lou, *Angew. Chem. Int. Ed.* **2021**, *60*, 11841.

- [40] C. Wei, Z. Feng, G. G. Scherer, J. Barber, Y. Shao-Horn, Z. J. Xu, *Adv. Mater.* **2017**, *29*, 1606800.
- [41] H. Yang, Y. Liu, S. Luo, Z. Zhao, X. Wang, Y. Luo, Z. Wang, J. Jin, J. Ma, *ACS Catal.* **2017**, *7*, 5557.
- [42] K. Guo, Y. Wang, J. Huang, M. Lu, H. Li, Y. Peng, P. Xi, H. Zhang, J. Huang, S. Lu, C. Xu, *ACS Catal.* **2021**, *11*, 8174.
- [43] S. Liu, B. Zhang, Y. Cao, H. Wang, Y. Zhang, S. Zhang, Y. Li, H. Gong, S. Liu, Z. Yang, J. Sun, *ACS Energy Lett.* **2023**, *8*, 159.
- [44] P. Wang, C. Li, S. Dong, X. Ge, P. Zhang, X. Miao, R. Wang, Z. Zhang, L. Yin, *Adv. Energy Mater.* **2019**, *9*, 1900788.
- [45] D. Y. Chung, P. P. Lopes, P. Farinazzo Bergamo Dias Martins, H. He, T. Kawaguchi, P. Zapoli, H. You, D. Tripkovic, D. Strmcnik, Y. Zhu, S. Seifert, S. Lee, V. R. Stamenkovic, N. M. Markovic, *Nat. Energy* **2020**, *5*, 222.
- [46] J. N. Hausmann, P. W. Menezes, *Appl. Catal. B* **2024**, *342*, 123447.
- [47] Y. Wang, Y. Zhao, L. Liu, W. Qin, S. Liu, J. Tu, Y. Qin, J. Liu, H. Wu, D. Zhang, A. Chu, B. Jia, X. Qu, M. Qin, *Adv. Mater.* **2022**, *34*, 2200088.
- [48] X. Han, H. Sheng, C. Yu, T. W. Walker, G. W. Huber, J. Qiu, S. Jin, *ACS Catal.* **2020**, *10*, 6741.
- [49] Y. Sun, X. Ren, S. Sun, Z. Liu, S. Xi, Z. J. Xu, *Angew. Chem. Int. Ed.* **2021**, *60*, 14536.
- [50] Y. Zhou, S. Sun, C. Wei, Y. Sun, P. Xi, Z. Feng, Z. J. Xu, *Adv. Mater.* **2019**, *31*, 1902509.
- [51] J. I. Orege, J. Wei, Q. Ge, J. Sun, *Nano Today* **2023**, *51*, 101914.
- [52] T. Wang, J. Wang, Y. Sun, Y. Duan, S. Sun, X. Hu, S. Xi, Y. Du, C. Wang, Z. J. Xu, *Appl. Catal. B* **2019**, *256*, 117844.
- [53] J. Wang, R. Gao, D. Zhou, Z. Chen, Z. Wu, G. Schumacher, Z. Hu, X. Liu, *ACS Catal.* **2017**, *7*, 6533.
- [54] Y. Pan, C. Zhao, A. Hu, R. Li, B. Zhou, Y. Fan, J. Chen, Z. Yan, C. Su, J. Long, *J. Colloid Interface Sci.* **2023**, *635*, 138.
- [55] T. Wang, Y. Sun, Y. Zhou, S. Sun, X. Hu, Y. Dai, S. Xi, Y. Du, Y. Yang, Z. J. Xu, *ACS Catal.* **2018**, *8*, 8568.
- [56] C. Mu, J. Mao, J. Guo, Q. Guo, Z. Li, W. Qin, Z. Hu, K. Davey, T. Ling, S. Qiao, *Adv. Mater.* **2020**, *32*, 1907168.
- [57] A. Hu, F. Li, W. Chen, T. Lei, Y. Li, Y. Fan, M. He, F. Wang, M. Zhou, Y. Hu, Y. Yan, B. Chen, J. Zhu, J. Long, X. Wang, J. Xiong, *Adv. Energy Mater.* **2022**, *12*, 2202432.
- [58] M. He, C. Shu, A. Hu, R. Zheng, M. Li, Z. Ran, J. Long, *Energy Storage Mater.* **2022**, *44*, 452.
- [59] A. Hu, M. Zhou, T. Lei, Y. Hu, X. Du, C. Gong, C. Shu, J. Long, J. Zhu, W. Chen, X. Wang, J. Xiong, *Adv. Energy Mater.* **2020**, *10*, 2002180.
- [60] Y. Qiao, H. Yang, Z. Chang, H. Deng, X. Li, H. Zhou, *Nat. Energy* **2021**, *6*, 653.
- [61] B. Yang, Y. Pan, T. Li, A. Hu, K. Li, B. Li, L. Yang, J. Long, *Energy Storage Mater.* **2024**, *65*, 103124.
- [62] R. Li, Y. Fan, C. Zhao, A. Hu, B. Zhou, M. He, J. Chen, Z. Yan, Y. Pan, J. Long, *Small Methods* **2023**, *7*, 2201177.
- [63] M. Balaish, J. Jung, I. Kim, Y. Ein-Eli, *Adv. Funct. Mater.* **2020**, *30*, 1808303.
- [64] K.-X. Wang, Q.-C. Zhu, J.-S. Chen, *Small* **2018**, *14*, 1800078.
- [65] H. Wang, X. Wang, M. Li, L. Zheng, D. Guan, X. Huang, J. Xu, J. Yu, *Adv. Mater.* **2020**, *32*, 2002559.
- [66] J. Chen, R. Li, B. Li, A. Hu, M. He, B. Zhou, Y. Fan, Z. Yan, Y. Pan, B. Yang, T. Li, K. Li, B. Li, J. Long, *J. Colloid Interface Sci.* **2024**, *657*, 384.
- [67] Y. Yan, Z. Ran, T. Zeng, X. Wen, H. Xu, R. Li, C. Zhao, C. Shu, *Small* **2022**, *18*, 2106707.
- [68] A. Hu, C. Shu, C. Xu, J. Li, R. Liang, R. Zheng, M. Li, Z. Ran, J. Long, *Chem. Eng. J.* **2020**, *382*, 122854.
- [69] A. Hu, W. Lv, T. Lei, W. Chen, Y. Hu, C. Shu, X. Wang, L. Xue, J. Huang, X. Du, H. Wang, K. Tang, C. Gong, J. Zhu, W. He, J. Long, J. Xiong, *ACS Nano* **2020**, *14*, 3490.
- [70] R. Li, A. Hu, C. Zhao, B. Zhou, M. He, Y. Fan, J. Chen, Z. Yan, Y. Pan, J. Long, *Chem. Eng. J.* **2023**, *452*, 139162.
- [71] C. Zhao, J. Long, B. Zhou, R. Zheng, M. He, R. Li, Y. Pan, A. Hu, C. Shu, *J. Mater. Chem. A* **2022**, *10*, 17267.
- [72] L. Liu, Y. Liu, C. Wang, X. Peng, W. Fang, Y. Hou, J. Wang, J. Ye, Y. Wu, *Small Methods* **2022**, *6*, 2101280.
- [73] Q. Xia, D. Li, L. Zhao, J. Wang, Y. Long, X. Han, Z. Zhou, Y. Liu, Y. Zhang, Y. Li, A. A. Adam, S. Chou, *Chem. Sci.* **2022**, *13*, 2841.
- [74] L. Lyu, S. Cho, Y.-M. Kang, *EES. Catal.* **2023**, *1*, 230.
- [75] X. Xie, B. Wang, Y. Wang, C. Ni, X. Sun, W. Du, *Chem. Eng. J.* **2022**, *428*, 131160.
- [76] Y. Zhou, S. Sun, C. Wei, Y. Sun, P. Xi, Z. Feng, Z. J. Xu, *Adv. Mater.* **2019**, *31*, 1902509.
- [77] Z. Wang, J. Huang, L. Wang, Y. Liu, W. Liu, S. Zhao, Z. Liu, *Angew. Chem. Int. Ed.* **2022**, *61*, DOI 10.1002/anie.202114696.
- [78] L. Ren, X. Wen, D. Du, Y. Yan, H. Xu, T. Zeng, C. Shu, *Chem. Eng. J.* **2023**, *462*, 142288.
- [79] D. Zhao, R. Zhang, M. Dai, H. Liu, W. Jian, F. Bai, X. Wu, *Small* **2022**, *18*, 2107268.
- [80] J. O. Olowoyo, R. J. Kriek, *Small* **2022**, *18*, 2203125.
- [81] F. Yang, X. Gao, J. Xie, X. Liu, J. Jiang, X. Lu, *Small Structures* **2021**, *2*, 2100144.
- [82] P. Shah, A. Unnarkat, F. Patel, M. Shah, P. Shah, *Process. Safe. Environ.* **2022**, *161*, 703.
- [83] Y. Zhang, Y. Hu, Z. Wang, T. Lin, X. Zhu, B. Luo, H. Hu, W. Xing, Z. Yan, L. Wang, *Adv. Funct. Mater.* **2020**, *30*, 2004172.
- [84] J. Zhang, X. Shang, H. Ren, J. Chi, H. Fu, B. Dong, C. Liu, Y. Chai, *Adv. Mater.* **2019**, *31*, 1905107.
- [85] Y. Li, J. Qin, Y. Ding, J. Ma, P. Das, H. Liu, Z.-S. Wu, X. Bao, *ACS Catal.* **2022**, *12*, 12765.
- [86] Z. Lian, Y. Lu, S. Ma, Z. Li, Q. Liu, *Chem. Eng. J.* **2022**, *445*, 136852.
- [87] S. Chakrabarty, A. Mukherjee, W.-N. Su, S. Basu, *Int. J. Hydrogen Energy* **2019**, *44*, 1565.
- [88] W. Liu, J. Bao, L. Xu, M. Guan, Z. Wang, J. Qiu, Y. Huang, J. Xia, Y. Lei, H. Li, *Appl. Surf. Sci.* **2019**, *478*, 552.
- [89] F. Zhu, J. Zhang, B. Yang, X. Shi, C. Lu, J. Yin, Y. Yu, X. Hu, *J. Alloys Compd.* **2018**, *749*, 433.
- [90] H. Fang, T. Huang, D. Liang, M. Qiu, Y. Sun, S. Yao, J. Yu, M. M. Dinesh, Z. Guo, Y. Xia, S. Mao, *J. Mater. Chem. A* **2019**, *7*, 7328.
- [91] P. C. Nagajyothi, K. Pavani, R. Ramaraghavulu, J. Shim, *Int. J. Hydrogen Energy* **2023**, *54*, S0360319923046050.
- [92] T. Ling, M. Jaroniec, S. Qiao, *Adv. Mater.* **2020**, *32*, 2001866.
- [93] J. Song, C. Wei, Z.-F. Huang, C. Liu, L. Zeng, X. Wang, Z. J. Xu, *Chem. Soc. Rev.* **2020**, *49*, 2196.
- [94] L. Ren, R. Zheng, D. Du, Y. Yan, M. He, Z. Ran, M. Li, C. Shu, *Chem. Eng. J.* **2022**, *430*, 132977.
- [95] Y. Zhu, Z. Wang, J. Gao, R. Sun, L. Yin, C. Wang, Z. Zhang, *Inorg. Chem. Front.* **2023**, *10*, 4252.
- [96] H. Lv, C. Fan, X. Xu, C. Zhao, J. Long, *J. Alloys Compd.* **2023**, *953*, 170130.
- [97] Y. Pan, K. Li, A. Hu, C. Zhao, Y. Zhang, X. Jiang, B. Li, J. Wang, J. Long, *Chem. Eng. J.* **2023**, *477*, 147209.
- [98] Y. Fan, R. Li, C. Zhao, A. Hu, B. Zhou, Y. Pan, J. Chen, Z. Yan, M. Liu, M. He, J. Liu, N. Chen, J. Long, *J. Colloid Interface Sci.* **2023**, *645*, 439.
- [99] H. Liang, H. Xiang, R. Zhu, C. Liu, Y. Jia, *J. Mater. Chem. A* **2021**, *9*, 14566.
- [100] Z. Liu, Z. Kong, S. Cui, L. Liu, F. Wang, Y. Wang, S. Wang, *Small* **2023**, *19*, 2302216.
- [101] Y. Zhang, Y. Chen, R. Liu, X. Wang, H. Liu, Y. Zhu, Q. Qian, Y. Feng, M. Cheng, G. Zhang, *InfoMat* **2023**, *5*, e12375.
- [102] X. Liu, L. Zhao, H. Xu, Q. Huang, Y. Wang, C. Hou, Y. Hou, J. Wang, F. Dang, J. Zhang, *Adv. Energy Mater.* **2020**, *10*, 2001415.
- [103] J. Zheng, X. Peng, Z. Xu, J. Gong, Z. Wang, *ACS Catal.* **2022**, *12*, 10245.
- [104] Z.-L. Jiang, G.-L. Xu, Z. Yu, T.-H. Zhou, W.-K. Shi, C.-S. Luo, H.-J. Zhou, L.-B. Chen, W.-J. Sheng, M. Zhou, L. Cheng, R. S. Assary, S.-G. Sun, K. Amine, H. Sun, *Nano Energy* **2019**, *64*, 103896.
- [105] J. Li, C. Shu, C. Liu, X. Chen, A. Hu, J. Long, *Small* **2020**, *16*, 2001812.
- [106] L. Ren, R. Zheng, B. Zhou, H. Xu, R. Li, C. Zhao, X. Wen, T. Zeng, C. Shu, *Small* **2021**, *17*, 2104349.
- [107] K. Song, X. Hu, W. Gao, Z. Liu, H. Qiao, T. Ishizaki, X. Shen, *J. Alloys Compd.* **2022**, *898*, 162774.
- [108] J. Li, C. Shu, A. Hu, Z. Ran, M. Li, R. Zheng, J. Long, *Chem. Eng. J.* **2020**, *381*, 122678.
- [109] D. Chen, R. Yu, R. Lu, Z. Pu, P. Wang, J. Zhu, P. Ji, D. Wu, J. Wu, Y. Zhao, Z. Kou, J. Yu, S. Mu, *InfoMat* **2022**, *4*, e12287.
- [110] Y. Du, B. Li, G. Xu, L. Wang, *InfoMat* **2023**, *5*, e12377.
- [111] Y. Wu, H. Ding, T. Yang, Y. Xia, H. Zheng, Q. Wei, J. Han, D. Peng, G. Yue, *Adv. Sci.* **2022**, *9*, 2200523.
- [112] Y. Zhang, S. Zhang, J. Ma, A. Huang, M. Yuan, Y. Li, G. Sun, C. Chen, C. Nan, *ACS Appl. Mater. Interfaces* **2021**, *13*, 39239.
- [113] P. Zhang, S. Zhang, M. He, J. Lang, A. Ren, S. Xu, X. Yan, *Adv. Sci.* **2017**, *4*, DOI 10.1002/advs.201700172.
- [114] Y. Zhao, L. Ding, X. Wang, X. Yang, J. He, B. Yang, B. Wang, D. Zhang, Z. Li, *J. Alloys Compd.* **2021**, *861*, 157945.
- [115] S. Guo, J. Wang, Y. Sun, L. Peng, C. Li, *Chem. Eng. J.* **2023**, *452*, 139317.
- [116] H. Xu, J. Yuan, G. He, H. Chen, *Coord. Chem. Rev.* **2023**, *475*, 214869.
- [117] J. Li, *Nano-Micro Lett.* **2022**, *14*, 112.
- [118] J. K. Nørskov, F. Abild-Pedersen, F. Studt, T. Bligaard, *Proc. Natl. Acad. Sci. USA* **2011**, *108*, 937.

- [119] W. Qu, Z. Tang, S. Tang, H. Wen, J. Fang, Q. Lian, D. Shu, C. He, *Adv. Funct. Mater.* **2023**, *33*, 2301677.
- [120] J. Wu, X. Wang, W. Zheng, Y. Sun, Y. Xie, K. Ma, Z. Zhang, Q. Liao, Z. Tian, Z. Kang, Y. Zhang, *J. Am. Chem. Soc.* **2022**, *144*, 19163.
- [121] J. Suntivich, H. A. Gasteiger, N. Yabuuchi, H. Nakanishi, J. B. Goodenough, Y. Shao-Horn, *Nat. Chem.* **2011**, *3*, 546.
- [122] Y. Sun, X. Ren, S. Sun, Z. Liu, S. Xi, Z. J. Xu, *Angew. Chem. Int. Ed.* **2021**, *60*, 14536.
- [123] Y. Li, H. Jiang, Z. Cui, S. Zhu, Z. Li, S. Wu, L. Ma, X. Han, Y. Liang, *J. Phys. Chem. C* **2021**, *125*, 9190.
- [124] J. Hwang, R. R. Rao, L. Giordano, Y. Katayama, Y. Yu, Y. Shao-Horn, *Science* **2017**, *358*, 751.
- [125] Y. Sun, H. Liao, J. Wang, B. Chen, S. Sun, S. J. H. Ong, S. Xi, C. Diao, Y. Du, J.-O. Wang, M. B. H. Breese, S. Li, H. Zhang, Z. J. Xu, *Nat. Catal.* **2020**, *3*, 554.
- [126] Z.-Q. Liu, K. Xiao, Y. Wang, P. Wu, L. Hou, *Angew. Chem. Int. Ed.* **2023**, *62*, e202301408.
- [127] Y. Zhou, S. Sun, J. Song, S. Xi, B. Chen, Y. Du, A. C. Fisher, F. Cheng, X. Wang, H. Zhang, Z. J. Xu, *Adv. Mater.* **2018**, *30*, 1802912.

Manuscript received: December 25, 2023

Revised manuscript received: February 12, 2024

Accepted manuscript online: February 16, 2024

Version of record online: March 7, 2024